

---

## Chapter 5

# Over-the-air testing of wireless devices in heavily loaded reverberation chambers

*Kate A. Remley<sup>1</sup>, Chih-Ming Wang<sup>2</sup>, and Robert D. Horansky<sup>1</sup>*

---

In many ways, what makes a “good” reverberation-chamber configuration for wireless over-the-air (OTA) tests that require signal demodulation is the opposite of what makes a good chamber configuration for EMC and EMI applications. For EMC/EMI tests, we strive for a highly reverberant, high Q environment with as little unstirred energy as possible to efficiently expose the device under test (DUT), on average, to the same isotropic, Gaussian-distributed field using a minimum number of mode-stirring states. Even though the DUT is not instantaneously exposed to the same field on a frequency-by-frequency basis, with a well-stirred chamber set-up the fields should, theoretically, be identically distributed when averaged over a mode-stirring sequence. The isotropy of the fields can be verified with a goodness-of-fit test to confirm that the magnitude of the fields are Rayleigh distributed. As well, providing the minimum loading to obtain the well-stirred condition [1] usually ensures excellent spatial uniformity when measured samples are averaged over a mode-stirring sequence, reducing the criticality of device placement in the chamber (subject to the constraints of the working volume for the specific reverberation-chamber configuration at a given frequency of interest).

On the other hand, for OTA testing, we often intentionally load the chamber with significantly more RF absorber than that required to meet the well-stirred condition in order to replicate the flat-fading channel conditions that wireless-device equalizers are designed to accommodate. Figure 5.1 illustrates this, where we see that a significant amount of absorbing material is needed to measure the correct value of receiver sensitivity, as indicated by the plateau in the value of total isotropic sensitivity (TIS). For smaller amounts of loading, the chamber set-up itself introduces distortion into the measurement [2-4]. This distortion obscures the goal of the OTA test, which is to assess the receiver’s performance. Once the channel is sufficiently flat, adding additional amounts of absorber does not significantly affect the mean value of the measured TIS, although the uncertainty due to lack of spatial uniformity may increase.

Seminal work in this area can be found in the literature, including [2-17]. Such loading is necessary to study device performance under conditions for which the

---

<sup>1</sup> Communications Technology Laboratory, U.S. National Institute of Standards and Technology

<sup>2</sup> Information Technology Laboratory, U.S. National Institute of Standards and Technology  
Work of the U.S. government, not subject to copyright in the United States.

device was designed to operate and where we wish to demodulate a communications signal having a finite instantaneous bandwidth (as opposed to the CW signals that are typically used in EMC/EMI tests). Loading reduces the Q and, because of an increase in unstirred energy, necessitates the use of position or antenna stirring. While it may be more complicated than for unloaded chambers, the goal of stirring sequence design in loaded reverberation chambers is to provide, on average, Gaussian-distributed fields in three dimensions, just as for the EMC/EMI test [16].

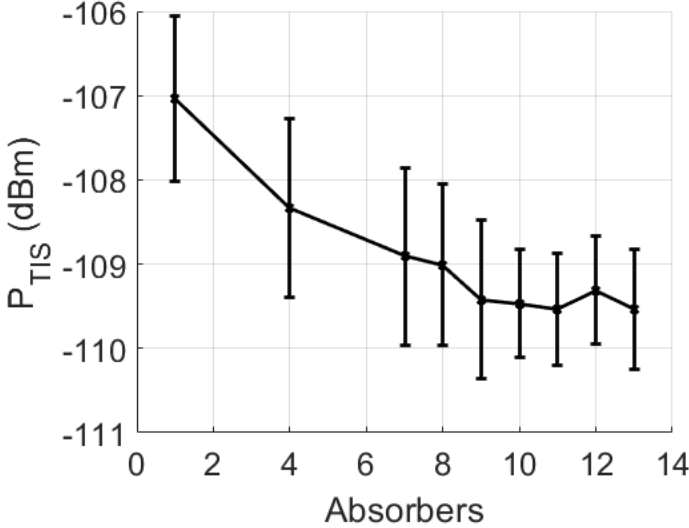


Figure 5.1: Received power corresponding to the receiver’s estimated total isotropic sensitivity ( $P_{TIS}$ ) as a function of chamber loading [17]. The metric  $P_{TIS}$  will be described in Section 5.5. Loading with eight absorbers corresponds to approximately 1% of the chamber volume, whereas the well-stirred condition may be achieved with a much lower amount (e.g., 0.11% in [1]). Even though absorbers will perform differently, these values provide an order-of-magnitude difference.

As we will discuss below, the significant amount of loading needed for wireless-device tests increases the correlation between measured frequency samples to provide the flat-fading channel. However, this also increases correlation between the positions of mechanical mode-stirrers, the locations of antennas, and even antenna orientations. Correlation reduces the number of independent samples in a reverberation-chamber measurement, which can significantly complicate the development of a stirring sequence that provides low uncertainty in the measurement of a quantity of interest. As such, quantifying correlation in the development of a stirring sequence and its effect on measurement uncertainty will be a large focus in this chapter.

In addition to chamber characterization and measurement uncertainty, we will also discuss types of wireless-device tests that are currently performed in loaded reverberation chambers. Here, we need to distinguish between two types of wireless-device OTA tests. The first is used by wireless industry organizations such as the CTIA and 3GPP [15] to assess specific metrics associated with device performance such as total radiated power (TRP) or total isotropic sensitivity [also called total

radiated sensitivity (TRS)]. These are standardized tests that allow labs having a variety of set-ups to obtain results comparable to an isotropic environment provided by an anechoic chamber. It is indeed counterintuitive to imagine that a highly reflective environment such as the reverberation chamber can provide channel conditions similar to an anechoic environment, but that is the goal of these tests. While the focus in this chapter is on cellular applications, the chamber characterization and tests discussed here are generally applicable to a wide variety of wireless technologies and to coexistence testing [18-21].

The second type of OTA wireless-device test conducted in heavily loaded reverberation chambers uses the reflective properties of the reverberation chamber to replicate specific multipath conditions. Loading is used to tune multipath decay times to those seen in real-world channels or to provide certain spatial channel characteristics specified by standards groups. Examples of these include replication of specific channels [8, 10, 22, 23, 63]; proposed tests for cellular handsets that use multiple-input, multiple-output (MIMO) antennas in which a channel emulator is used to replicate a specific multipath channel model and the MIMO antenna gain is measured [24-27]; and the implementation of 3D spatial channel models such as in [28].

The two types of tests have many similarities because they allow users to replicate specific channel conditions (for example, a specific power-delay profile, power-angle spectrum, or an isotropic channel). The distinction is that the former, isotropic channel, is designed to test wireless device performance under conditions for which it was designed. The latter, more realistic, channel conditions may stress the wireless device in unexpected ways. After a discussion of the chamber characterization steps that must be considered for both isotropic and more realistic multipath OTA test conditions, we will discuss each of these applications with a focus on the former because these tests are currently standardized.

## 1.1 Chamber Characterization for OTA Tests

For many EMC/EMI tests, the spatial uniformity of the chamber set-up is first evaluated by performing measurements of orthogonal field components at multiple locations throughout the working volume of the chamber. Samples of the fields measured at a specific location are averaged over a mode-stirring sequence, which is often carried out by movement of mechanical mode stirrers. If the variation of the averaged fields measured at the locations within the working volume is sufficiently low, then the user may perform the measurement at a single location within the working volume. For a chamber set-up satisfying the well-stirred condition, having Gaussian-distributed real and imaginary field components, the uncertainty related to the mode-stirring process ideally decreases by  $1/\sqrt{N}$ , where  $N$  is the number of uncorrelated mode-stirring samples [29] in a stepped (static-channel) mode-stirring sequence.

Let us distinguish here between the small amount of loading that may be used under the “well-stirred condition” described in [1] and Chapter 2 of this book, and the (typically) heavier loading required for demodulating communication signals with defined instantaneous bandwidths. For clarity, we shall refer to the latter as “heavily loaded” reverberation chambers throughout this chapter. The amount of loading needed to demodulate the communications signal without significant

chamber-induced distortion depends on the bandwidth and transmission format of the signal to be demodulated. “Spread spectrum” signals cover the entire communications channel during transmission. In these cases, loading is used to create a coherence bandwidth that meets or exceeds the signal bandwidth [15, 17, 30]. Examples include the signals utilized in the wideband code-division multiple access (W-CDMA) transmission format, which have a bandwidth of 3.84 MHz, and the 22 MHz 802.11b wireless local-area-network (WLAN) waveform, which contains a modulated signal that is spread over the entire communications channel. Such waveforms require chamber loading to achieve 3.84 MHz or 22 MHz. On the other hand, the OFDM transmission format is designed to mitigate frequency selective fading by use of many separate subcarriers, where each subcarrier is sufficiently narrowband to experience frequency-flat fading in high multipath environments. For the OFDM case, little loading may be needed [15, 30, 31].

In such heavily loaded reverberation chambers, we typically must use a combination of mode-stirring mechanisms that both alter the boundary conditions (e.g., mechanical-paddle stirring) and move the device under test (DUT) to various locations within the chamber (e.g., antenna-position or “platform” stirring) to account for the decreased spatial uniformity caused by the RF absorbing elements. Antenna-position stirring may consist of physical movement of the antenna on, for example, a rotating platform or linear translation stage or the use of multiple antennas at various locations and/or polarizations within the reverberation chamber. The need to perform averaging over many locations within the working volume is one differentiator of wireless test from traditional EMC/EMI test applications. Intimately related to this is the need to account for the increased correlation between mode-stirring samples in both the estimate of a quantity of interest and the corresponding measurement uncertainty.

In this section, we focus on methods for identifying correlations and optimizing stirring sequences to minimize correlation between samples. While correlated samples may be used to estimate a quantity of interest, designing a stirring sequence to minimize correlation between mode-stirring samples increases the efficiency of a measurement by requiring the acquisition of fewer overall samples.

We start with an introduction to the basic set-up used for testing wireless devices, including a derivation of the important chamber metric called the “reference power transfer function,”  $G_{\text{Ref}}$ . The metric  $G_{\text{Ref}}$  characterizes the loss in the chamber set-up. It is written as a gain so that losses take on negative values on a decibel scale. An accurate estimate of the chamber loss is important for obtaining calibrated power-based metrics such as total radiated power. While  $G_{\text{Ref}}$  itself may be derived from S-parameter measurements made with a vector network analyzer (VNA), the power-based DUT metrics themselves require calibration with a power-measurement instrument such as a power meter, spectrum analyzer, or base-station emulator (BSE).

$G_{\text{Ref}}$  is also a convenient metric for assessing the correlations between mode-stirring samples in a chamber set-up, as well as for obtaining various components of uncertainty. Our derivation of  $G_{\text{Ref}}$  is followed by a description of the effects of loading on the electromagnetic properties within the chamber, such as spatial uniformity and the distribution of samples under loaded conditions. This is followed by a discussion of methods to identify the correlation between samples, both in terms of frequency and location within the chamber. Finally, we discuss the metrics of  $K$ -

factor, which describes the level of unstirred energy relative to stirred energy in a chamber, and isotropy, including methods for characterizing isotropy in heavily loaded reverberation chamber set-ups. These two metrics,  $K$ -factor and isotropy, may be used to assess different characteristics of a chamber set-up.

The techniques presented in this section are intended to provide straight-forward methods for optimally configuring heavily loaded reverberation chambers for wireless-device tests, in terms of both accuracy and efficiency in a measurement.

### *5.1.1 Configuring a Reverberation Chamber for Wireless Device Testing*

While some parameters such as antenna efficiency may be determined from relative measurements of gain or loss, power-based metrics such as TRP and TIS report an absolute power value. For these measurements, it is essential to have a good estimate of the chamber's reference power transfer function  $G_{\text{ref}}$ .  $G_{\text{ref}}$  is measured in a separate step from the DUT measurement (usually with a VNA) and is corrected for (calibrated out) during the calculation of power-based performance metrics. For example, to measure the total radiated power from a cellular-enabled device, the device is placed in the reverberation chamber and commanded over-the-air by the base-station emulator to transmit at full power. For each step in the stirring sequence, the BSE will measure the DUT's power minus the chamber's loss. Thus, to obtain the correct value of TRP in post processing, it is necessary to account for the power that was lost in transmission through the chamber,  $G_{\text{ref}}$ .

The reference measurement,  $G_{\text{ref}}$ , is intended to estimate the chamber's transfer function as experienced by the DUT's transmitted and received signals. Because most wireless devices have integrated antennas, the reference measurement is generally performed with a reference antenna that is different from the DUT's antenna. However, the radiation pattern of the reference antenna is typically selected to be similar to that of the DUT (for example, both azimuthally omnidirectional antennas) so that it is exposed to a similar set of mode-stirred fields as the DUT during the stirring sequence.

#### **5.1.1.1 Chamber Set-Up**

A commonly used [4, 14, 15] two-step procedure for testing wireless devices in reverberation chambers is illustrated in Figure 5.2(a) and (b). The procedure consists of the measurement of the chamber's reference power transfer function [the "reference measurement," shown in Figure 5.2(a)] and the DUT measurement [shown in Figure 5.2(b)]. Samples are acquired by the measurement antenna at each stepped mode-stirring state and are averaged to yield an estimate of the quantity of interest, to within a desired uncertainty.

The two set-ups look very similar to each other, with the primary difference being the measurement instruments used: a VNA is used for the reference measurement and a BSE is used for the DUT measurement. In Figure 5.2(a) and 2(b), two metallic mode-stirring paddles change the boundary conditions in the chamber and a rotating turntable, on which both the DUT and the reference antenna sits, steps

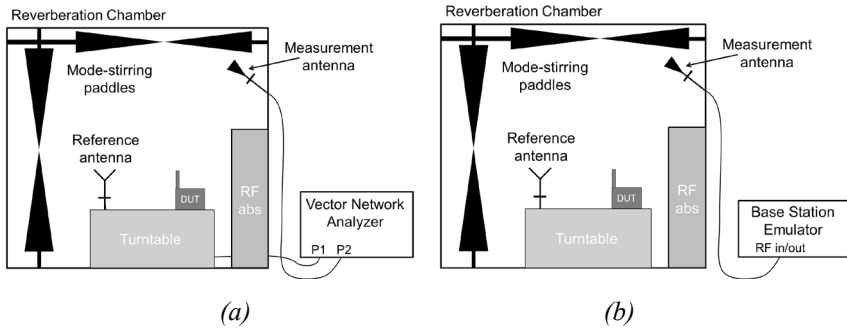


Figure 5.2: Common configuration for wireless device measurements in a reverberation chamber, including two rotating paddles, RF absorber to broaden the coherence bandwidth, and a rotating platform on which the DUT and the reference antenna are placed. In (a), a VNA measures the reference power transfer function and in (b), a base station emulator measures the performance of the DUT. The reference plane of the VNA in (a) are denoted by the line at the base of the antennas.

through various angles. At each step, a mode-stirring sample is acquired via the measurement antenna.

Because the average spatial uniformity of the mode-stirred fields is less constant in a heavily loaded chamber than in a chamber designed to meet the well-stirred condition, it is important that the chamber configuration for the reference and DUT measurements be as similar to each other as possible to minimize uncertainty in the measurement. For example, the placement of the turntable, RF absorber, fixtures, and measurement antenna should be the same for both measurements. The reference and DUT antennas should be exposed to the same nominal stirring sequence, although they may be placed anywhere within the working volume of the chamber (that is, the region that has been bounded by a separate set of characterization measurements), which is why Figure 5.2 shows them both placed concurrently for both measurement setups on the turntable but not in exactly the same physical locations.

The reference measurement shown in Figure 5.2(a) is carried out with a VNA that acquires a full set of  $S$  parameters between the reference antenna and the measurement antenna at the measurement reference planes indicated by a short perpendicular line on each antenna.

In addition to the rotating paddles and platforms shown in Figure 5.2, other types of mode-stirring might be employed, including horizontal and/or vertical translation of mechanical paddles, translation of the DUT itself, multiple sampling antennas located at various locations and/or at different polarizations within the chamber, and movable walls.

Because an OTA test requires frequency averaging over the band of the modulated signal, frequency stirring, per se, is not typically considered as a separate stirring mechanism. While frequency stirring and frequency averaging consist of the same procedure (averaging mode-stirred samples over a specified frequency band),

the wireless community often views frequency averaging as a necessary part of computing a power-based metric – by averaging over the channel bandwidth – rather than as part of the stirring sequence.

All mode-stirring mechanisms are not created equal in terms of efficient stirring of the fields, as we will discuss in Section 5.1.4. However, the use of rotating paddles and platform stirring, as shown in Figure 5.2, are common stirring mechanisms and, without loss of generality, we will use them to illustrate concepts related to OTA wireless-device test.

### 5.1.1.2 The Reference Power Transfer Function

The chamber's reference power transfer function  $G_{\text{ref}}$  is determined by averaging over a stepped mode-stirring sequence during the reference measurement. It is then calibrated out during the calculation of the power-based metric. The value of  $G_{\text{ref}}$  may be estimated from  $S$ -parameter measurements as [14, 24]

$$G_{\text{Ref}} = \frac{\langle |S_{21,\text{Ref}}|^2 \rangle_{N_W}}{\eta_M \eta_R (1 - |\Gamma_M|^2)(1 - |\Gamma_R|^2)} \quad (5.1)$$

where  $G_{\text{Ref}}$  is the estimate of the reference power transfer function,  $\eta_x$  is the efficiency of the measurement ( $x = M$ ) or reference ( $x = R$ ) antenna [see Figure 5.2(a)] and the term  $\Gamma_x$  corresponds to the free-space reflection coefficient of each of the two antennas, which may be measured in an anechoic or reverberation chamber. If measured in a reverberation chamber, the chamber must be unloaded (or lightly loaded) condition. See [32] for more detail. Note that the implicit frequency dependence is suppressed to simplify the expression. To compute  $G_{\text{Ref}}$ , the ensemble average is taken over  $N_W$  stepped mode-stirring samples ( $N_W$  samples *within* a stirring sequence). Refer to [14] for a detailed derivation of this expression, where expressions for choices of reference planes other than those shown in Figure 5.2(b) are derived.

Multiple *independent realizations* of  $G_{\text{Ref}}$  (each denoted below as  $G_{\text{Ref},p}$ ) are often acquired to estimate the uncertainty due to lack of spatial uniformity. The independent realizations consist of mode-stirring sequences whose mode-stirring samples are uncorrelated from sequence to sequence, to be discussed in Section 5.1.4.

The independent realizations may be averaged to improve the estimate of the chamber's reference power transfer function. The average may be written as

$$\hat{G}_{\text{Ref}} = \frac{1}{N_B} \sum_{p=1}^{N_B} G_{\text{Ref},p}, \quad (5.2)$$

where  $p$  denotes an independent realization and measurements are made over  $N_B$  independent realizations of the mode-stirring sequence ( $N_B$  samples *between* stirring sequences). The multiple independent realizations are primarily used to obtain the component of uncertainty due to lack of spatial uniformity, derived from the standard deviation taken over the  $N_B$  positions as

$$\sigma_{G_{\text{Ref}}} = \sqrt{\frac{1}{N_B - 1} \sum_{p=1}^{N_B} (G_{\text{Ref},p} - \hat{G}_{\text{Ref}})^2}. \quad (5.3)$$

The value  $\sigma_{G_{\text{Ref}}}$  is often used as a metric for evaluating the lack of spatial uniformity in a heavily loaded reverberation chamber, with the component of uncertainty

corresponding to  $\sigma_{G_{\text{Ref}}}/\sqrt{N_B}$ . This will be discussed further in Section 5.4 on uncertainty.

Typically, the DUT antenna will not be identical to the reference antenna, in terms of radiation pattern. This means that the ratio of unstirred energy to stirred energy (the  $K$ -factor) may be different for the reference and DUT measurements, over and above the expected spatially dependent uncertainty that is captured by  $\sigma_{G_{\text{Ref}}}$ . This, in turn, may result in different correlations and added uncertainties. To minimize this effect, current practice is to select a reference antenna that produces a  $K$ -factor that is similar to that of the DUT. For example, omnidirectional reference antennas are often used to estimate  $G_{\text{Ref}}$  for cellular device testing. A discussion of uncertainty related to this effect is discussed in [33], which is summarized in Section 5.4.3.

The reference power transfer function  $G_{\text{Ref}}$ , derived from the complex  $S_{21}$ , may be used to determine the power delay profile (power-based response in time) of the reverberation chamber set-up. For the  $n$ th stepped mode-stirring position, which can be considered to have been measured at delay,  $\tau_n$ , the impulse response of the chamber set-up may be estimated from the inverse Fourier transform of the measured  $S$  parameters  $h_n(t) \cong \text{IFT}\{S_{21}(f, n)\}$ . The magnitude squared of the impulse response corresponds to the power delay profile ( $PDP$ ) [10]

$$PDP(t) = \langle |h(t, \tau_n)|^2 \rangle, \quad (5.4)$$

where  $h(t, \tau_n)$  is the  $n$ th mode-stirring sample of the linear, time-varying impulse response of the channel and the brackets denote the ensemble average. The RMS delay spread is found from the square root of the second central moment of the  $PDP$  as

$$\tau_{\text{RMS}} = \sqrt{\frac{\int_0^\infty (t - t_0)^2 PDP(t) dt}{\int_0^\infty PDP(t) dt}}, \quad (5.5)$$

where  $t_0$  is the mean delay of the propagation channel for step  $n$  given by

$$t_0 = \frac{\int_0^\infty t PDP(t) dt}{\int_0^\infty PDP(t) dt}. \quad (5.6)$$

This time-domain representation of the chamber's reference power transfer function can be useful in several applications, as will be discussed in Section 5.1.3 on coherence bandwidth and Section 5.3 on replicating specific multipath channels in reverberation chambers.

### 5.1.2 Distribution of Mode-Stirring Samples in Loaded Chambers

Both the reference power transfer function and the  $S$  parameters themselves will, ideally, follow specific distributions. In chambers loaded to meet the well-stirred condition, the samples often follow these distributions without the need for position stirring. In heavily loaded chambers, assessing the degree to which the distribution



of samples follows the theoretical value is a good diagnostic to understand whether a stirring sequence contains a sufficient number of independent mode-stirring samples.

As discussed in previous sections, there are three complex, orthogonal components of the electric field vector,  $E_i = E_{i1} + jE_{i2}$ , where  $i = x; y; z$ . When sampled over many mode-stirring samples, each component of the complex electric field vector may be represented by a complex Gaussian distribution. For “noninvasive” antennas (typically those that are physically small relative to the chamber volume), the chamber may be characterized by measuring the  $S$  parameters over the stepped mode-stirring sequence with a VNA, instead of measuring the electric field. If we measure the chamber’s complex transfer function (proportional to  $S_{21}$ ) with a VNA, the real and imaginary components will also, ideally, both be Gaussian distributed. Further, the magnitude of  $S_{21}$  will be Rayleigh distributed and the magnitude squared ( $|S_{21}|^2 \propto G_{\text{Ref}}$ ) will be exponentially distributed [1, 29, 34, 35].

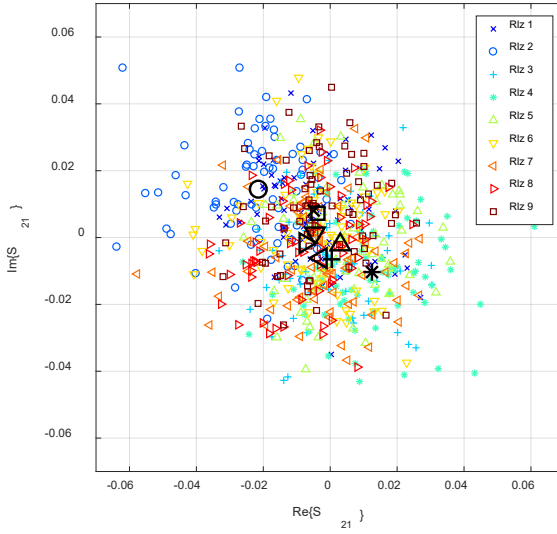
As we have seen in previous chapters, in a well-stirred chamber, the distribution of measured mode-stirring samples can be nearly ideal if it is obtained under conditions that include: a sufficient number of mode-stirring samples; little direct coupling between antennas; a high-Q chamber set-up; the use of effective, uncorrelated mechanical mode-stirring mechanisms [1, 35].

However, for a heavily loaded chamber, obtaining the desired distribution can be more complicated. When a large amount of RF absorbing material is present in the chamber, some of the energy introduced into the chamber is not randomized through mechanical mode-stirring. This increases correlation between measured mode-stirring samples, including those acquired at different frequencies, antenna orientations, locations, and paddle positions. This, in turn, reduces the effective number of samples in the chamber. Use of an inadequate number of uncorrelated samples in a mode-stirring sequence can lead to an incorrect estimate of the quantity of interest and an underestimate of its uncertainty.

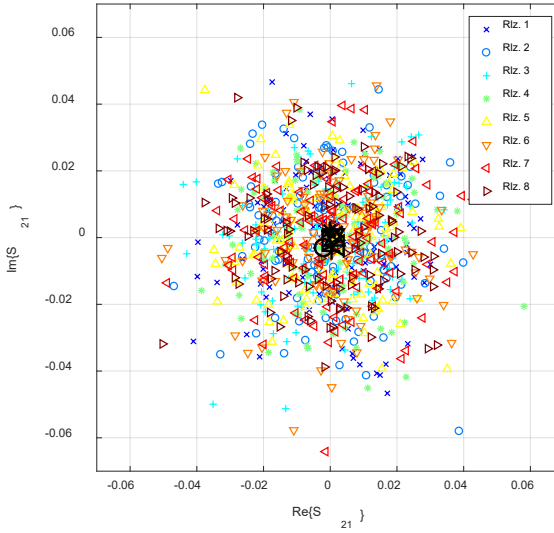
Physically, in a heavily loaded chamber, the lack of spatial uniformity of the measured, averaged fields due to the absorbers increases the correlation between the mode-stirring samples. If measurements are made in one location within a heavily loaded chamber, the distributions may be less ideal, for example, resulting in a non-zero mean in the Gaussian distribution of the real and imaginary components of the measured  $S_{21}$ . Such a non-zero mean can be visualized as an offset from the origin when the real and imaginary components of the complex transmission coefficient are plotted in polar form (see, e.g., [8, 36]). However, such an offset is negligible under well-stirred conditions, which may be different for lightly and heavily loaded chamber set-ups because of the need for position stirring in the heavily loaded chamber.

An illustration of the importance of position stirring for heavily loaded chambers is shown in Figure 5.3, which plots  $\text{Im}(S_{21})$  versus  $\text{Re}(S_{21})$  samples from a stepped mode-stirring sequence for a heavily loaded chamber. The loading was chosen to provide a coherence bandwidth of approximately 4 MHz. This corresponds to 0.46 m<sup>3</sup> of RF absorber in a 45.2 m<sup>3</sup> chamber, or roughly 1% of the chamber’s volume. In Figure 5.3(a), antenna-position stirring of the reference (transmit) antenna was used, while in Figure 5.3(b) no position stirring was used. Measurements were made for  $N_B = 8$  [Figure 5.3(a)] or  $N_B = 9$  [Figure 5.3(b)] independent realizations of the

stirring sequence. Independent realizations correspond to those for which the same nominal stirring sequence is used (e.g., nine different sets of 10 paddle and 10



(a)



(b)

Figure 5.3: Scatter plot of complex  $S_{21}$  data at 2 GHz measured in a chamber that was heavily loaded for a CBW of approximately 4 MHz (a) with position stirring and (b) without position stirring. Note the mean values, given by the thick, black symbols, are clustered at the origin for (a) but not (b).

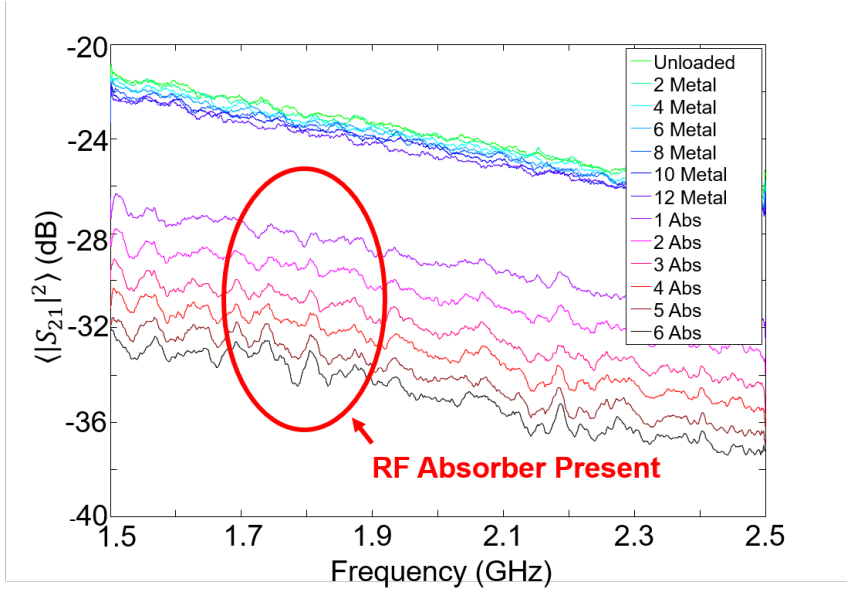


Figure 5.4: Relative mean power  $\langle |S_{21}|^2 \rangle$  as a function of loading. The top curves show a chamber with metallic boxes (labeled “2 Metal” through “12 Metal”) The lower curves (circled in red) show the chamber in the same configuration but with RF absorber labeled “1 Abs” through “6 Abs.” RF absorber loading increases the average insertion loss in the chamber, which can be calibrated out.

antenna positions), and for which correlation between the mode-stirring samples has been minimized, as described in sections that follow.

As can be seen in Figure 5.3(a), the measured values of  $\text{Re}(S_{21})$  and  $\text{Im}(S_{21})$  are closely distributed around the origin with the mean values of the eight independent realizations of the stirring sequence clustered at the origin. The magnitude of the real and imaginary components of  $S_{21}$  in Figure 5.3(a) are smaller than they would be in an unloaded chamber because fields within the heavily loaded chamber interact with RF absorber and decay before they arrive at the receive antenna. This decrease in received signal can be calibrated out with a reference measurement made under the same loading conditions and with the same (or similar) antennas as are used in the DUT measurement [33].

The case in Figure 5.3(b) utilizes similar loading conditions as the case in Figure 5.3(a) but no position stirring was used. We see that mean values of  $\text{Re}(S_{21})$  and  $\text{Im}(S_{21})$  are less-well clustered around the origin in Figure 5.3(b), illustrating the reduction in spatial uniformity of the averaged fields within the chamber’s working volume. This highlights the importance of position stirring in loaded reverberation chambers.

Physically, the decrease in spatial uniformity can be attributed in part to a faster decrease in the “stirred energy” relative to the “unstirred energy” in the heavily

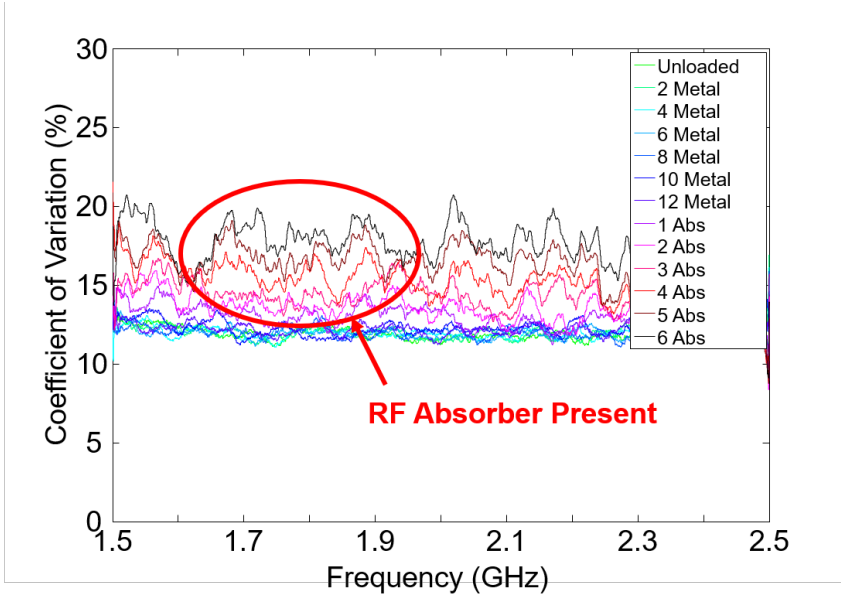


Figure 5.5: The coefficient of variation calculated for eleven monopoles placed throughout a loaded reverberation chamber for metallic and absorbing material.

loaded chamber. That is, the fields that undergo mode-stirring have a greater chance of interacting with an absorber as they travel between transmit and receive antennas than do the fields that do not interact with mode-stirring mechanisms. Thus, the unstirred components, which remain fixed for specific frequencies and/or positions within the chamber, become relatively more important with loading, introducing correlation between mode-stirring samples and decreasing spatial uniformity. This effect of decreased stirred energy relative to the unstirred energy as a function of loading is described by the Rician  $K$ -factor, sometimes referred to as simply  $K$ -factor. This metric is discussed in Section 5.1.6.

The decrease in the magnitude of the reference power transfer function with increased chamber loss is further illustrated in Figure 5.4 [37]. The top set of curves shows the “relative mean power,” defined as  $\langle |S_{21}|^2 \rangle$ , for chamber loading with an increasing number of large, stacked metallic boxes having a maximum surface area of approximately  $5.8 \text{ m}^2$ . The bottom set of curves show  $\langle |S_{21}|^2 \rangle$  for stacked RF absorber of similar physical dimensions, (maximum surface area of approximately  $6.2 \text{ m}^2$ ). Measurements were made over the frequency range from 1.5 GHz to 2.5 GHz, utilizing 72 rotating-paddle mode-stirring positions. In the experiment, eleven monopole receive antennas were located throughout the chamber. The results in Figure 5.4 are for one of these locations. The transmit antenna was a broadband dual-ridge horn antenna aimed at the rotating paddle.

Figure 5.4 shows that for loading with reflective material, the power insertion loss does not change significantly even for the maximum surface area. However, when RF absorbers having a surface area values similar to the metal boxes are placed

within the chamber, the values of  $\langle |S_{21}|^2 \rangle$  significantly decrease as a function of loading.

To quantify the decrease in the spatial uniformity of the chamber, we consider the standard deviation of the relative power samples  $|S_{21}|^2$  measured at the eleven monopole antennas for the different loading configurations. The absolute standard deviation is not independent from the mean. For this reason, we use a normalized measure, called the coefficient of variation, where

$$C_v = \frac{\sigma}{\mu} \times 100 \%, \quad (5.7)$$

where  $\sigma$  = standard deviation and  $\mu$  = mean received power over the number of antenna locations for a given loading configuration (11 in this example). Figure 5.5 shows the coefficient of variation increases with RF absorber loading, unlike loading with metallic objects.

The increased variance as a function of frequency with loading – fundamentally caused by increased correlation between mode-stirring samples – must be accounted for when optimizing the stirring sequence in order to minimize uncertainty and maximize efficiency in determining power-based metrics such as total radiated power or total isotropic sensitivity. In the following sections, we discuss methods for identifying and quantifying correlation as a function of frequency and in terms of spatial locations within a loaded reverberation chamber.

### 5.1.3 Coherence Bandwidth

Understanding the correlation between various mode-stirred samples in a heavily loaded reverberation chamber is the key to performing OTA tests with low uncertainty. Much effort has been expended by the community to understand the effects of frequency correlation and to account for it in the determination of uncertainty [2, 4, 13, 38], especially for standardized certification tests such as those whose goal is to emulate an isotropic environment [15].

As mentioned above, loading is necessary to create correlation between frequencies within the chamber in order to provide a channel for which the device was designed operate. If the channel is not sufficiently flat over the bandwidth of the modulated communication signal, the chamber set-up itself will artificially introduce distortion, masking the potential distortion from the DUT that the OTA test has been developed to uncover.

The effect of increased loading as a function of frequency is illustrated in Figure 5.6. In Figure 5.6, we show the chamber's power response,  $G_{\text{Ref}}$ , versus frequency across a 4 MHz communication channel bandwidth for an increasing number of RF absorbers for a single mode-stirring sequence step (*i.e.*, a static channel with specific paddle orientations, turntable location, and antenna polarizations). The figure shows a decrease in fluctuation as a function of frequency as more loading is added to the chamber. The chamber response for each loading case has been offset by arbitrary values to make the graph easier to read.

A common metric that allows assessment of the amount of the frequency flattening provided by a given loading case is the coherence bandwidth (CBW). The CBW was originally used in RF propagation channel modelling, describing the frequency separation necessary for two signals to be considered statistically

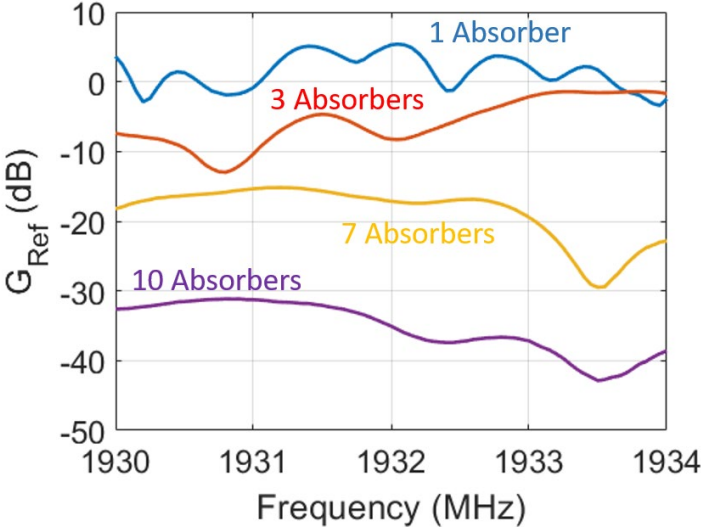


Figure 5.6: The chamber power response,  $G_{\text{Ref}}$ , across a 4 MHz communication-channel bandwidth for increasing numbers of absorbers [17]. Curves are offset by arbitrary decibel values to clearly illustrate the variation as a function of frequency.

independent [39]. This metric assesses the frequency selectivity of a channel. A wider CBW corresponds to a smoother frequency response. The CBW has an inverse relationship to the quality factor of a reverberation chamber and is similar to the average mode bandwidth (AMB) metric  $f/Q(f)$  described in previous chapters. That is, the more that a reverberation chamber configuration stores energy, the more frequency selective the chamber set-up is.

The CBW may be defined by the autocorrelation function,  $R$ , as given by

$$R(i, n) = \frac{\sum_{j=1}^{M-1} S_{21}(f_{j,n}) S_{21}^*(f_{j+i,n})}{\sum_{j=1}^{M-1} S_{21}(f_{j,n}) S_{21}^*(f_{j,n})}, \quad (5.8)$$

where  $S_{21}(f_j, n)$  corresponds to the measured complex  $S_{21}$  at frequency step  $f_j$  with  $M$  frequency points measured within the bandwidth of interest,  $BW$ , so that  $f_1 = f_c - \frac{BW}{2}$  and  $f_M = f_c + \frac{BW}{2}$ . The index,  $n$ , is the mode-stirring sample (out of  $N_w$ ). The index,  $i$ , corresponds to one of several frequency-step offsets (lags) over the bandwidth of interest (here  $BW = 100$  MHz [15]) where  $-(M-1) \leq i \leq (M-1)$ . The frequency lag for a set of measured data will be given by,  $\Delta f = i \left( \frac{f_M - f_1}{M-1} \right)$ . The asterisk denotes complex conjugation. The bandwidth,  $BW$ , is taken over 100 MHz to provide stable results, as has been shown previously [40]. The calculation of CBW is similar to that of the “first-order autocorrelation” of [1]. For lightly loaded chambers, assessing correlation between two adjacent frequency steps provides a metric to judge the effectiveness of mode-stirring in a given chamber set-up. For the heavy loading required in wireless device testing, correlation is studied on further adjacent frequencies.

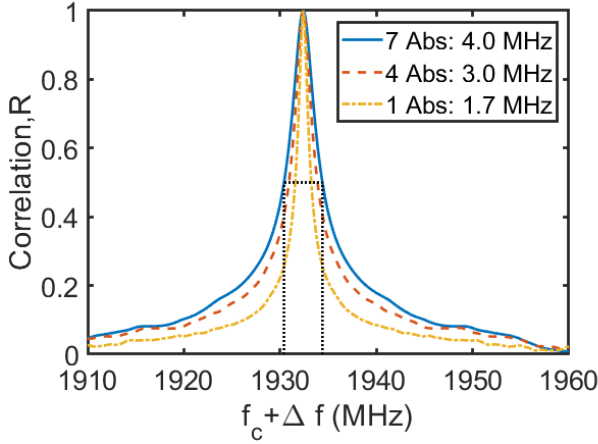


Figure 5.7: The frequency correlation function for a chamber loaded with three different amounts of RF absorber.

A representative set of CBW plots for loading with various amounts of RF absorber is shown in Figure 5.7. The CBW is computed for a defined threshold of the autocorrelation function. The width for a threshold of 0.5 is illustrated by the dotted line in Figure 5.7 for the 7-absorber case. In current practice, *e.g.*, [15], the CBW would be chosen to meet or exceed the modulation bandwidth of the communication signal being tested. The choice of this threshold can be derived by understanding that the CBW is the Fourier-space equivalent of the root-mean-square (RMS) delay spread  $\tau_{\text{RMS}}$ , which is a measure of the decay of power in the chamber as a function of time. It was defined in (5.5) in Section 5.1.1 and is inversely equivalent to the quality factor. If the temporal power in the chamber,  $P_\tau$ , follows an ideal exponential decay, it may be written as [41, 42]

$$P_\tau = S_0 e^{-\frac{\tau}{\tau_{\text{RMS}}}}, \quad (5.9)$$

for  $\tau \geq 0$ , where  $\tau$  is the time where the power is measured after injection at  $\tau = 0$  and  $S_0$  is an arbitrary magnitude. In this case, the frequency autocorrelation is the symmetric two-sided Fourier Transform, which is

$$R = \frac{S_0 \tau_{\text{RMS}}}{1 + j2\pi\Delta f \tau_{\text{RMS}}}. \quad (5.10)$$

In this case, the full-width at 0.5 threshold of the magnitude of  $R$  (the CBW) relates to the RMS delay spread as [2, 41, 42]

$$\text{CBW} = \frac{\sqrt{3}}{\pi \tau_{\text{RMS}}}. \quad (5.11)$$

Other threshold values may be used to define correlation depending on the application. For example, in the next subsection, we choose a threshold of 0.3 to

define spatial correlation in order to provide “independent realizations” of the stirring sequence.

#### 5.1.4 Spatial Correlation and the Mode-Stirring Sequence

As discussed above, loading is necessary for unimpaired demodulation of communication signals during OTA testing. Loading increases correlation between frequency components (as quantified by the coherence bandwidth discussed in Section 5.1.4), but also increases spatial correlation between mechanical paddle positions, antenna orientations, and platform positions [4, 13, 38, 43]. Correlation between mode-stirring samples can reduce measurement efficiency: In the best case, a stirring sequence with correlated samples may require more samples to obtain a desired level of uncertainty [6, 12, 34, 35, 44]. In the worst case, if there is no position stirring and the samples are highly correlated (as in a heavily loaded chamber), it may not be possible to measure the quantity of interest with sufficient accuracy for certain applications. Therefore, this section focuses on techniques to develop and verify “optimal” mode-stirring sequences.

Prior work in the literature has discussed identification of spatially uncorrelated samples. For assessing spatial correlation between stepped mode-stirring samples *within* a stirring sequence, sample linear autocorrelation is often used [4, 12, 34, 44]. The correlation *between* two mode-stirring sequences sample cross correlation (such as Pearson’s cross correlation) is often used [2, 15, 44]. This latter statistic estimates the linear dependence between two realizations of a given mode-stirring sequence and is sometimes used to determine if these realizations may be considered “independent.” Multiple independent realizations are used to quantify the uncertainty due to lack of spatial uniformity for a given chamber set-up. These two techniques are next described, with examples of their use in OTA test applications.

##### 5.1.4.1 Correlation Within a Measurement

To identify the physical step size for a specific mode-stirring mechanism beyond which we deem samples to be uncorrelated, the linear autocorrelation is often used. This metric assesses the relative change in mode-stirring samples within a proposed stirring sequence (*e.g.*, are samples less correlated if we use one large paddle rotating in 3° steps or two smaller paddles rotating with 2° steps). From the sample linear autocovariance, we may identify, for example, the “coherence angle” for platform stirring, or the “coherence length” for linear translation. The correlation may also be determined for the case of multiple mode-stirring mechanisms used simultaneously. The better the stirring mechanisms are at randomizing (or, more accurately, statistically altering) the fields in the chamber, the smaller the coherence distance between samples.

The sample linear autocorrelation across mode-stirring samples may be found from  $S$ -parameter measurements as

$$R_{CA}(f, i) = \frac{\sum_{j=1}^{N_w-i} (S_{21}(f, n_j) - \langle S_{21}(f, n) \rangle_{N_w}) (S_{21}(f, n_{j+i}) - \langle S_{21}(f, n) \rangle_{N_w})^*}{\sum_{j=1}^{N_w} (S_{21}(f, n_j) - \langle S_{21}(f, n) \rangle_{N_w}) (S_{21}(f, n_j) - \langle S_{21}(f, n) \rangle_{N_w})^*}, \quad (5.12)$$

where  $\langle S_{21}(f, n) \rangle_{N_w}$  is the mean of the  $S_{21}$  measurement at frequency,  $f$ , over the mode-stirring sequence,  $N_w$ . As with coherence bandwidth, the normalization term in the denominator provides a maximum value of one. By subtracting the mean, we may evaluate the relative effectiveness of a stirring mechanism on the stirred energy.



The effect of unstirred energy on the measurement is evaluated from the uncertainty due to lack of spatial uniformity, described briefly in Section 5.1.1, and in more detail in Section 5.4.2.

Linear autocorrelation (5.12) operates on the entire mode-stirring sequence by calculating the correlation coefficient from a copy of itself shifted one step (lag) away, which is repeated until the entire sequence has been shifted from the first to the last point in the sequence. The minimum step size between “uncorrelated samples” corresponds to the set of samples physically spaced farther than those for which the correlation coefficient falls below the specified threshold. This technique is very similar to the calculation of coherence bandwidth discussed above. And, as with coherence bandwidth, correlation between samples in a reverberation chamber is a function of the loading and the frequency of operation.

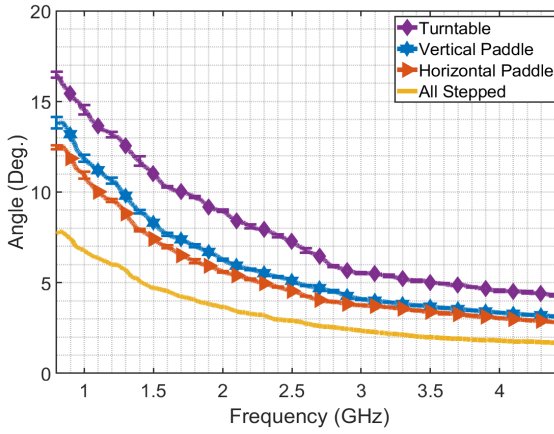
Linear autocorrelation (5.12) characterizes the spatial correlation between mode-stirring samples within a stirring sequence and, thus, may be used to judge the relative effectiveness of various mode-stirring mechanisms. This makes it useful in developing optimized stirring sequences in which spatial correlation is minimized. The concept is illustrated in Figure 5.8(a) and 8(b), which show correlation between mode-stirring samples for various stirring mechanisms as a function of frequency in an unloaded chamber [Figure 5.8(a)] and a loaded chamber [Figure 5.8(b)]. The various stirring mechanisms are evaluated separately and in groups, allowing the user to identify the spatial step requirements of each.

For this large (4.27 m x 3.65 m x 2.90 m) chamber, the available mechanical mode-stirring mechanisms included two rotating paddles and a rotating platform. We conducted measurements of each mode-stirring mechanism separately, collecting samples over uniform angular steps for stirring sequences in which (1) only the horizontal paddle was stepped; (2) only the vertical paddle was stepped; (3) only the rotating turntable was stepped; (4) all three were stepped (the “All Stepped” case in the legend); and (5) both paddles were stepped together (only for the loaded case). The spatial acquisition step size was chosen to be well below the expected coherence angle in order to develop correlation curve (similar to Figure 5.7):  $1^\circ$  for all mechanisms, except for the All Stepped case which was  $3^\circ$ .

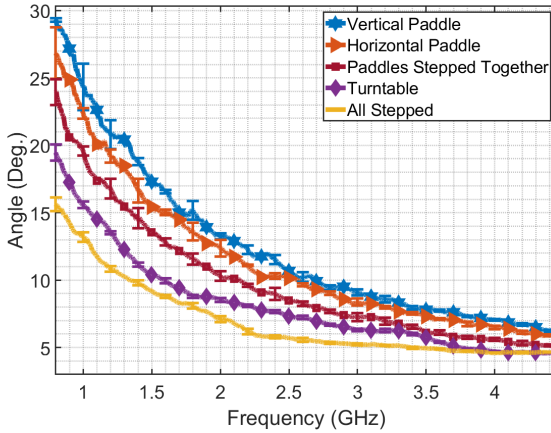
At each center frequency of interest, we applied (5.12) to the complex  $S_{21}$  data over a 100 MHz bandwidth and applied a threshold of 0.3 to this curve to estimate the minimum step size for each mode-stirring mechanism. At least four independent realizations were collected for each mode-stirring mechanism (except the unloaded All Stepped Case) to create the error bars.

Note that the threshold of 0.3 provides a more stringent requirement for samples to be deemed uncorrelated than would a threshold of 0.5 (commonly used for coherence bandwidth). As the threshold value decreases, the coherence-angle values become larger. This reduces potential correlation between samples, but also can limit the number of uncorrelated samples that is possible to obtain within a chamber’s working volume. That is, if the turntable coherence angle for a heavily loaded chamber is  $10^\circ$ , only 36 turntable samples may be used in the stepped mode-stirring sequence. This can affect the user’s ability to develop multiple independent realizations for the uncertainty analysis and is a topic of current research.

Several effects may be noted for the unloaded chamber configuration in Figure 5.8(a). First, for all frequencies, the smaller coherence angle for the horizontal paddle indicates that it provides more efficient mode stirring than the vertical paddle. This



(a)



(b)

Figure 5.8: Coherence angle determined as a function of frequency for a large reverberation chamber which was (a) unloaded (CBW of approximately 613 kHz) and (b) loaded for a 3.2 MHz CBW. Individual stirring mechanisms and combinations are utilized for the mode-stirring sequences, including the vertical paddle only; horizontal paddle only; two paddles together; turntable only; and all three of these mechanisms stepped simultaneously (All Stepped).

makes sense due to its larger physical size (a cylinder tracing out a volume of  $2.97\text{m}^3$  as compared to  $2.27\text{m}^3$  for the vertical paddle). A second effect to note is that the wider coherence angle for the turntable means that the turntable provides the least-effective individual stirring mechanism of the three. This is due to both the absence of significant boundary condition changes as compared to paddle stirring and the high value of spatial uniformity in the large, unloaded chamber. That is, the mode-

stirring effectiveness of an antenna moving on the turntable through the relatively uniform spatial environment of the unloaded chamber is less than the mode-stirring effectiveness provided by the paddles.

Finally, the smallest coherence angles occur between samples for the All Stepped case, indicating, as expected, that this is the most efficient mode-stirring sequence. For example, an optimized stirring sequence at 2 GHz could consist of mode-stirring samples in which the two paddles and the platform each rotate in approximately  $4^\circ$  steps, providing approximately 90 uncorrelated stepped mode-stirring samples.

For the loaded chamber case shown in Figure 5.8(b), the correlation between mode-stirring samples is significantly higher. Again, the large (horizontal) paddle is shown to be more effective at mode stirring by its smaller coherence angle (relative to the other mode-stirring mechanisms). The figure clearly illustrates the importance of position stirring in loaded-chamber configurations because the coherence angle for the turntable is now the single most effective mechanism. Physically, position stirring allows the antenna to sample the peaks and nulls within the reduced-uniformity environment.

Finally, note that the All Stepped case at 2 GHz indicates that angular steps of approximately  $7^\circ$  would be required to obtain uncorrelated samples, as compared to  $4^\circ$  for the unloaded chamber.

Measurements such as these provide a straightforward method for assessing the correlation between mode-stirring mechanisms within a chamber configuration in order to derive an optimal stirring sequence. More advanced methods such as principle component analysis have been investigated in [45] and are the subject of current research.

#### 5.1.4.2 Correlation Between Measurements

While autocovariance approaches may be used to evaluate samples within a mode-stirring sequence, cross-correlation methods are typically used for evaluating spatial correlation between independent realizations of a mode-stirring sequence. Sample cross correlation, sometimes referred to as Pearson's cross-correlation function [2], may be determined from  $S$ -parameter measurements made for two independent realizations  $a$  and  $b$  of the same mode-stirring sequence as

$$R_{AB}(f) = \left| \frac{\sum_{n=1}^{N_W} \left[ (s_{21,a} - \langle s_{21,a} \rangle_{N_W}) (s_{21,b} - \langle s_{21,b} \rangle_{N_W})^* \right]}{\sqrt{\sum_{n=1}^{N_W} \left[ |s_{21,a} - \langle s_{21,a} \rangle_{N_W}|^2 \right]} \sqrt{\sum_{n=1}^{N_W} \left[ |s_{21,b} - \langle s_{21,b} \rangle_{N_W}|^2 \right]}} \right| \quad (5.13)$$

Pearson's illustrates spatial correlation between pairs of mode-stirring sequences as a function of frequency, averaged over the  $N_W$  values in the mode-stirring sequence. Generally, (5.13) is applied to all pairs of realizations of a mode-stirring sequence to determine the correlation between measurements or independent realizations, verifying their independence.

As an example of the application of (5.13) in OTA wireless test, in [15], Pearson's cross correlation is applied to measurements of  $G_{\text{Ref}}$  to determine whether the reference antenna is in too close of proximity to a lossy DUT. Close placement of an antenna near an RF absorbing material can block the radiation pattern of the

antenna, causing a systematic underestimate in the determination of  $G_{\text{Ref}}$  [46, 47]. The problem is that there is no way to know in advance how lossy a DUT may be. For example, a metal cellular-enabled parking meter in close proximity may not alter the radiation pattern the reference antenna, whereas a lossy section of a foam-enclosed car dashboard may present a significant change in the pattern. The test plan in [15] was designed to be sufficiently general to allow chamber pre-configuration and pre-characterization to measure both of these devices accurately.

The procedure in [15] requires the user to insert a block of RF absorber having a surface area as large (or larger) as the largest DUT to be measured. Because very few wireless devices will be as lossy as RF absorber, this scenario is expected to provide a worst-case simulated lossy DUT. The user then performs a measurement of  $G_{\text{Ref}}$  with the reference antenna placed a nominal distance from the RF absorber. This measurement is followed by a second, *spatially uncorrelated* measurement made closer to the block of RF absorber. As long as the change in  $G_{\text{Ref}}$  due to its closer proximity to the simulated DUT does not exceed a specified threshold, its nominal location is deemed to be sufficiently far from any DUT having a surface area of that size or smaller.

This procedure is illustrated in Figures 5.9(a) and (b), where an azimuthally omnidirectional reference antenna was placed 34.5 cm [Figure 5.9(a)] and 19.5 cm [Figure 5.9(b)] from the block, respectively.

Figure 5.10 shows the results of application of (5.13) to the measured complex  $S_{21}$  data for the frequency band covering 1.85 GHz to 2.0 GHz (the Personal Communications or PCS Band in the United States). A threshold of 0.3 correlation has been plotted as a horizontal red bar on the graph. The cross correlation between the two locations for nine different turntable positions is shown, where the stirring sequence consists of mechanical paddle stirring only (a non-ideal stirring sequence used to illustrate the spatial correlation effect).

The figure shows that the turntable positions exhibit better correlation at higher frequencies, where the data lie below the 0.3 threshold line (with one exception). At

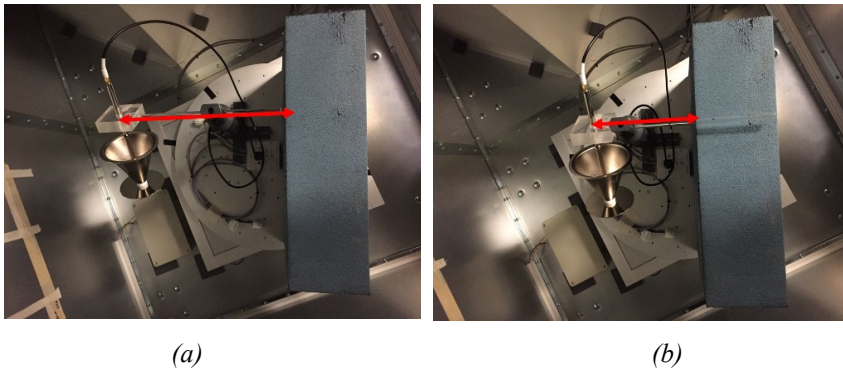


Figure 5.9: Top view looking down on a discone reference antenna placed (a) 34.5 cm and (b) 19.5 cm from a block of RF absorber to study the “Proximity effect.” The block of absorber is intended to simulate a worst-case lossy DUT.

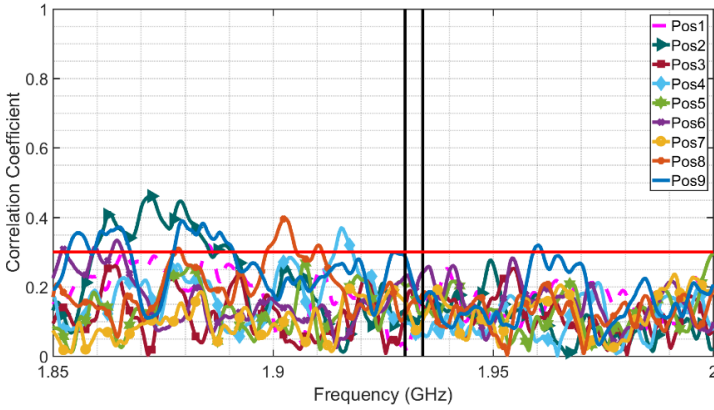


Figure 5.10: Pearson's cross correlation function applied to a pair of  $G_{Ref}$  measurements made at two distances from an RF absorbing block to study the "Proximity Effect" of [15].

lower frequencies, there are more frequencies where correlation between antenna locations exists. The black vertical lines indicate a 3.84 MHz W-CDMA cellular communication channel. For this example, the user would be recommended to place the reference antenna somewhat farther from the simulated lossy DUT for the reference measurement to ensure that the reference antenna does not significantly couple directly into the DUT. The need to assess and minimize spatial correlation is a clear illustration of the statistical nature of the reverberation chamber, and, again, the importance of position stirring in heavily loaded chambers.

### 5.1.5 Lack of Spatial Uniformity Due to Loading

The metric  $\sigma_{G_{Ref}}$ , derived in (5.3) (Section 5.1.1), may be used to quantify the lack of spatial uniformity in a heavily loaded reverberation chamber [4, 40]. The localized placement of RF absorber dampens the modes at specific locations, reducing the spatial uniformity of the stirred energy throughout the chamber. Because the TRP and TIS are derived from distributions of samples that should ideally have specific distributions (see Section 5.1.2), understanding the lack of spatial uniformity is essential for designing an adequate stepped mode-stirring sequence.

For OTA measurements of wireless devices, the uncertainty in the estimate of TRP or TIS is often dominated by the lack of spatial uniformity [4, 14], as will be discussed in Section 5.4.1. In fact, uncertainty derived from (5.3) has been adopted by the wireless community in standardized test methods that utilize heavily loaded reverberation chambers [15].

To assess the uncertainty due to lack of spatial uniformity for a given chamber configuration and stirring sequence, one may perform measurements of multiple independent realizations of the proposed stirring sequence, where independence can be evaluated by use of the cross-correlation procedure in (5.13) of Section 5.1.4. The procedure is similar to, but somewhat more complicated than, the method for

assessing spatial uniformity in [48]. For wireless device test, the chamber is first loaded for a desired coherence bandwidth and, typically, a stirring sequence is developed to minimize correlation between mode-stirring samples. The chamber's reference power transfer function is then measured with several different independent realizations of the same stirring sequence, where each sequence uses the same number of paddle angles, antenna positions, etc., but the samples are nominally spatially uncorrelated from one implementation to the next, as confirmed using (5.13). The standard deviation between these independent realizations is then computed from (5.3) with  $N_B - 1$  degrees of freedom [49]. The value of  $\sigma_{G_{\text{Ref}}}$  will depend on the chamber configuration and the types of mode stirring used in the stirring sequence.

Often nine or more independent realizations are required for standardized OTA tests [15]. To increase the number of independent realizations of stirring sequences, users often elect to use mechanisms such as polarization stirring (where the antenna is moved to one of three orthogonal polarizations during the multiple realizations of the stirring sequence), linear position stirring (where a linear translation stage moves the antenna up-and-down or side-to-side within the chamber), and/or multiple-antenna stirring (where multiple measurement antennas are placed at uncorrelated locations within the chamber, each recording its own version of the mode-stirred samples). A method for optimizing independent samples is presented in Section 5.4.2. The stirring sequence must enable a sufficiently low value of (5.3) so that the combined uncertainty (see Section 5.4.3) is below a specified value for the chamber configuration (including the stirring sequence) to be deemed acceptable for use in OTA tests.

### 5.1.6 *Isotropy for Loaded Chambers*

An ideal reverberation chamber set-up will theoretically provide an “isotropic” electromagnetic environment [35], where the fields impinge on the receive antenna from all angles of incidence equally when averaged over the collection of mode-stirring states in a mode-stirring sequence. Real reverberation chamber environments will naturally be anisotropic and characterizing the level of anisotropy is often a key figure of merit in standardized test procedures. Typically, to characterize anisotropy through measurement, the magnitude-squared of either the electric field or the transmission parameter  $S_{21}$  is considered [48, 50, 51]. To simplify notation, we use the field representation here.

The statistics used for current standardized isotropy validation tests [48] are based on measurements of the three orthogonal components of the electric field,  $E_i, i = x, y, z$  for each mode-stirring state. The real and imaginary components of the electric field may be represented by complex Gaussian distributions. We denote

$$E_i = E_{i_1} + jE_{i_2}. \quad (5.14)$$

Then  $E_{i_1} \sim N(\mu_{i_1}, \sigma_{i_1}^2)$  and  $E_{i_2} \sim N(\mu_{i_2}, \sigma_{i_2}^2)$  and  $E_{i_1}$  and  $E_{i_2}$  are independent. If we further assume that the in-phase and quadrature components have equal variances,

i.e.,  $\sigma_{i_1}^2 = \sigma_{i_2}^2 = \sigma_i^2$ , the magnitude squared of  $E_i$  is written as

$$|E_i|^2 = (\mu_{i_1} + Z_1\sigma_i)^2 + (\mu_{i_2} + Z_2\sigma_i)^2 \quad (5.15)$$

$$\begin{aligned} &= \sigma_i^2 \left[ \left( Z_1 + \frac{\mu_{i_1}}{\sigma_i} \right)^2 + \left( Z_2 + \frac{\mu_{i_2}}{\sigma_i} \right)^2 \right], \\ &= \sigma_i^2 W_i, \end{aligned} \quad (5.16)$$

where  $Z_1$  and  $Z_2$  are independent standard Gaussian random variables, and hence,  $W_i$  is distributed as a non-central  $\chi^2$  with 2 degrees of freedom and non-centrality parameter (e.g. see [52])

$$\lambda_i = \frac{\mu_{i_1}^2 + \mu_{i_2}^2}{\sigma_i^2}. \quad (5.17)$$

For stirred fields in a reverberation chamber, a definition for the statistical isotropy of the field may be given by the following equality

$$\langle |E_x|^2 \rangle = \langle |E_y|^2 \rangle = \langle |E_z|^2 \rangle, \quad (5.18)$$

where  $x, y$ , and  $z$  represent any three orthogonal orientations, and the average is taken over all mode-stirring samples. Given the result in (5.16), (5.18) reduces to

$$2\sigma_x^2 + \mu_{x_1}^2 + \mu_{x_2}^2 = 2\sigma_y^2 + \mu_{y_1}^2 + \mu_{y_2}^2 = 2\sigma_z^2 + \mu_{z_1}^2 + \mu_{z_2}^2.$$

If we further assume that the unstirred energy is sufficiently small, i.e., both  $\mu_{i_1}$  and  $\mu_{i_2} \ll \sigma_i$  for  $i = x, y, z$ , then (5.18) is equivalent to

$$\sigma_x^2 = \sigma_y^2 = \sigma_z^2 = \sigma^2. \quad (5.19)$$

Note that most stirring sequences used in wireless device tests utilize position stirring. Thus, when averaged over the stirring sequence, (5.19) will often be satisfied even for chamber configurations with significant amounts of unstirred energy at a single location. With (5.19), the distribution of  $|E_i|^2$  in (5.16) is

$$|E_i|^2 \sim \sigma^2 \chi_2^2 \quad (5.20)$$

where  $\chi_2^2$  is a central  $\chi^2$  distribution with 2 degrees of freedom. This distributional property of  $|E_i|^2$  in (5.20) can be used to develop statistical hypothesis tests for isotropy by comparing the observed and theoretical distributions of  $|E_i|^2$  using, for example, a chi-square goodness-of-fit test (e.g., see [53]). Note that, while the Anderson-Darling goodness-of-fit test may converge more quickly for continuous samples [35], the chi-square formulation is easy to use in standardized tests where specific distribution binning must be utilized between labs.

Since the distribution of  $|E_i|^2$  involves an unknown parameter  $\sigma$ , a common approach is to use ratios of  $|E_i|^2$  to develop test statistics. To simplify the notation, denote  $X = |E_x|^2$ ,  $Y = |E_y|^2$ , and  $Z = |E_z|^2$ . Then the ratios of  $X$ ,  $Y$ , and  $Z$  are ratios

of independent  $\chi^2$  random variables and are free of any unknown parameters. IEC 61000-4-21 [48] denotes anisotropy coefficients based on ratios of  $X$ ,  $Y$ , and  $Z$ . Specifically, planar and total field anisotropy coefficients  $A_{xy}$  and  $A_t$  are used:

$$A_{xy} = \frac{X-Y}{X+Y}, \quad A_{yz} = \frac{Y-Z}{Y+Z}, \quad A_{zx} = \frac{Z-X}{Z+X}, \quad (5.21)$$

$$A_t = \frac{1}{3} \sqrt{(A_{xy}^2 + A_{yz}^2 + A_{zx}^2)}. \quad (5.22)$$

Under (5.20),  $A_{xy}$ ,  $A_{xz}$ , and  $A_{yz} \sim \text{uniform}(-1, 1)$  (that is, have a uniform distribution ranging from  $-1$  to  $1$ ), and are correlated, that is, no two  $A_{ij}$  pairs are independent.

The distribution of  $A_t$  can be derived numerically from knowledge of the planar field-anisotropy-coefficient distributions, but it is also conveniently obtained by simulation. Figure 5.11 displays the CDF of the total anisotropy coefficient  $A_t$  based on 1,000,000 Monte Carlo samples.

The difference between the measured CDF of  $A_t$  and ideal CDF may be computed within the framework of the chi-square test to determine if the chamber is isotropic.

It can be shown by simulation that an isotropy validation test based on  $A_t$  tends to pass the test when the chamber exhibits a substantial level of anisotropy. To correct this deficiency, one may use any two coefficients  $A_{ij}$ ,  $i \neq j$ ,  $i, j = x, y, z$  to carry out the isotropy validation test. The problem is that these coefficients are not independent, and hence the exact significance level of such a test cannot be determined. Consequently, validation tests based on two independent test statistics that are functions of the ratios of  $X$ ,  $Y$ , and  $Z$  are desirable so that the correct

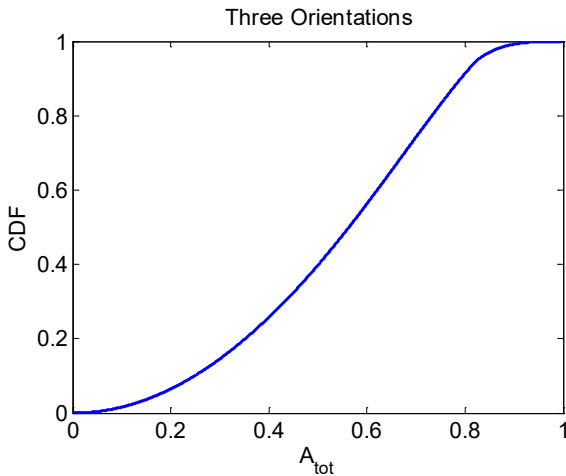


Figure 5.11: Cumulative distribution functions of  $A_t$  calculated with (5.22).



significance level of the tests can be determined and components that cause anisotropy can be identified. For example, test statistics  $X/(X + Y)$  and  $Z/(X + Y + Z)$  are independent under the hypothesis that the chamber is isotropic, and hence can be used for this purpose. The development of isotropy validation tests based on a pair of independent statistics that produce adequate powers in all anisotropy conditions and correct significance levels is a topic for future research.

### 5.1.7 *K-Factor and Decay Time*

The Rician  $K$ -factor, or simply  $K$ -factor, is a metric that is commonly used in the area of wireless communications to describe a reflective multipath channel. Specifically, it is the ratio of “discrete” multipath, in which a certain number of paths between the transmitter and receiver consist of specular, deterministic reflections, over the number of randomly scattered, “diffuse” multipath reflections [39]. For communications channels, specularly reflected signal paths are typically more desirable than diffuse multipath both because these paths usually provide stronger received signals and because they can be modeled analytically, and, thus, adaptive protocols in receivers can adjust appropriately. Consequently, high  $K$ -factor is often a desirable figure of merit for wireless communications.

Conversely, for traditional reverberation-chamber measurements, stirred energy is often equated with a well-performing set-up and, effectively, diffuse multipath, and is deemed desirable. In [8], the  $K$ -factor is defined as the ratio of the unstirred to stirred energy. That is,

$$K \approx \frac{| \langle S_{21} \rangle |^2}{\langle |S_{21} - \langle S_{21} \rangle|^2 \rangle}. \quad (5.23)$$

In this definition, the unstirred energy consists of the power after averaging over the mode-stirring sequence, denoted by the angled brackets. The denominator is the variance of the received power and yields an approximation of the stirred energy [8].

While there will always be a finite  $K$ -factor in a reverberation chamber due to losses in the metal and, if utilized, RF absorber, within this limit, minimization of the  $K$ -factor will minimize measurement errors and uncertainties. The value of the  $K$ -factor will depend on a number of measurement set-up parameters, including the dimensions of the chamber, the reflectivity of the chamber walls, the types of antennas used and their orientation with respect to each other, the number of mode-stirring samples, and, of course, the amount of RF absorber, as well as its placement within the chamber.

One can take simple steps to minimize the  $K$ -factor by eliminating the line-of-sight path and simple unstirred reflected paths between the measurement antenna and the DUT. For example, one can point the measurement antenna toward the mechanical mode stirrers within chamber and cross-polarize the measurement antenna with the DUT and reference antenna. Additionally, the use of a directional measurement antenna can help reduce line-of-sight interactions between the antenna and the DUT [4, 40].

Figure 5.12 shows that the  $K$ -factor increases as a function of loading. That is, for a given mode-stirring sequence, as the unstirred energy increases due to loading, so does the  $K$ -factor. In this figure, the  $K$ -factor was averaged over 72 paddle positions in a chamber with a single rotating paddle and no platform stirring. The

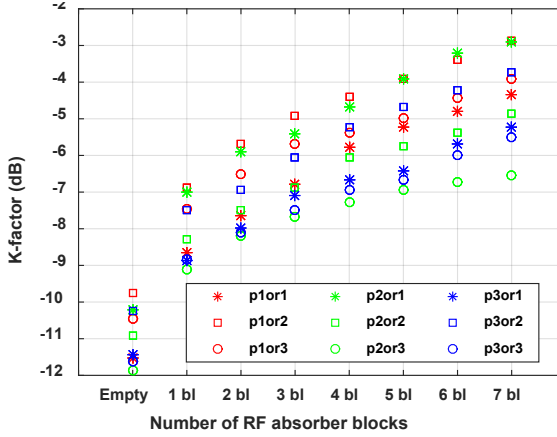


Figure 5.12: Rician  $K$ -factor calculated for measurements made at three omnidirectional transmit antenna locations and three orientations for each location. Results were averaged over the PCS band, 1.85 GHz – 2.0 GHz (from [40]).

legend refers to the “p” positions and “or” orientations of an omnidirectional reference antenna.

In Figure 5.12, it is interesting to note that the  $K$ -factor values can differ by 2 to 4 dB for various locations within the chamber due to lack of spatial uniformity (indicating different amounts of spatial correlation between locations). As well, for different frequency averaging bandwidths, different  $K$ -factors will be obtained for a particular chamber set-up, again due to the correlations between mode-stirring samples. Understanding the  $K$ -factor and the parameters that increase or decrease its value can help in the optimization of a stirring sequence and troubleshooting of an unanticipated measurement result.

### 5.1.8 Chamber Characterization: A Summary

For wireless device tests in which the signal must be demodulated, use of a loaded reverberation chamber is generally required to provide a channel that is flat enough to match that in which the device was designed to operate. Because loading degrades the spatial uniformity of the averaged fields in the chamber, measured samples are often correlated. We have presented several methods for assessing this correlation in terms of the necessary increase in frequency correlation (coherence bandwidth) and the less-desirable spatial correlation between mode-stirring samples. With these techniques, users may develop optimized mode-stirring sequences in which each sample contributes maximally to an improvement in the estimate of a quantity of interest. In the next section, we discuss the estimation through measurement of

power-based metrics that may be used to evaluate the OTA performance of many cellular-based wireless devices.

## 5.2 Over-the-Air Tests for Radiated Power and Receiver Sensitivity

Given a well-devised mode-stirring sequence based on knowledge of the correlations between mode-stirring samples, users can perform measurements and derive uncertainties for metrics such as those used by cellular-device certification groups, obtaining results comparable to anechoic chambers, which have traditionally been used for these tests [54]. Commonly used metrics are total radiated power (TRP), total isotropic sensitivity (TIS), data throughput, and channel capacity [40, 55, 56]. Here we focus on the two most basic tests that have been standardized used for single-input, single-output (SISO) wireless devices: TRP and TIS [15].

### 5.2.1 Total Radiated Power

TRP is one of the most fundamental metrics that can be obtained from OTA testing of a wireless device, as reported in the literature [48, 57, 58]. As mentioned previously, heavy chamber loading is not necessary for TRP measurements in reverberation chambers because there is no need to demodulate the signal. However, establishing a communication link by a BSE is typically necessary in cellular applications to control the DUT power output.. Also, many labs do load so that they can use the same chamber set-up and precharacterization for both TIS and TRP measurements.

The description of TRP here is consistent with the over-the-air test methodology that is utilized by the cellular industry [14, 15]. It corrects for impedance mismatch between the antennas and the chamber, as well as the antenna efficiencies. As in the chamber characterization steps of Section 5.1, these methods are based on “stepped mode-stirring” with samples collected under static conditions.

The objective in a TRP measurement is to estimate the total power radiated by the DUT in free space and the associated measurement uncertainty. Typically,  $G_{\text{Ref}}$  is first measured with a VNA, as illustrated in Figure 5.2(a). We then define  $P_{\text{Meas}}$  as the average power measured by the receiver over the occupied bandwidth of the modulated signal. The measurement is carried out at the reference plane indicated in Figure 5.2(b), where the power measurement instrument is the receiver section of a BSE.

In practice, for cellular device testing, the BSE establishes a communication link with the wireless device under test and instructs it to radiate at full power. Samples of the received power are measured at the reference plane of the receive antenna ( $P_{\text{Meas}}$  in (Pmeas)) by the BSE or other receiver. Each measured sample is corrected for the chamber set-up’s reference power transfer function  $G_{\text{Ref}}$ , the measurement antenna characteristics (mismatch and efficiency), impedance mismatch between the measurement antenna and receiver and cable loss (if applicable).

The TRP may then be estimated from the ensemble average of the  $P_{\text{Meas}}$  samples acquired over all  $N_W$  mode-stirring positions and  $N_B$  independent realizations, as given by

$$P_{\text{TRP}} = \frac{\langle P_{\text{Meas}} \rangle_{N_{\text{W}}N_{\text{B}}} |1 - \Gamma_{\text{M}} \Gamma_{\text{RX}}|^2}{G_{\text{Ref}} \eta_{\text{M}} (1 - |\Gamma_{\text{M}}|^2)}, \quad (5.24)$$

where,  $\eta_{\text{M}}$  is the efficiency of the measurement antenna,  $\Gamma_{\text{M}}$  is the free-space reflection coefficient of the measurement antenna,  $\Gamma_{\text{RX}}$  is the reflection coefficient of the base-station emulator or other receiver assembly (including cable, if used). Again, note that if the antenna efficiencies are measured in a reverberation chamber, it must be unloaded [32]. The chamber gain for the DUT measurement  $G_{\text{DUT}}$  is often estimated from the chamber reference measurement  $G_{\text{Ref}}$ , as described above.

In terms of measured quantities  $P_{\text{Meas}}$  and  $S_{21,\text{Ref}}$ , we have

$$P_{\text{TRP}} = \frac{\langle P_{\text{Meas}} \rangle_{N_{\text{W}}N_{\text{B}}} |1 - \Gamma_{\text{M}} \Gamma_{\text{RX}}|^2 \eta_{\text{R}} (1 - |\Gamma_{\text{R}}|^2)}{\langle |S_{21,\text{Ref}}|^2 \rangle_{N_{\text{W}}N_{\text{B}}}}, \quad (5.25)$$

where  $\langle |S_{21,\text{Ref}}|^2 \rangle$  is the ensemble average of the measured transmission parameter obtained during the reference measurement, frequency averaged over the bandwidth of the channel being tested. Note that the measurement antenna's mismatch-and-efficiency terms from (5.1) in Section 5.1.1 and (5.24) cancel, leaving only the reference antenna-efficiency-and-mismatch terms. In practice, the DUT measurement  $\langle P_{\text{Meas}} \rangle_{N_{\text{W}}N_{\text{B}}}$  is often made for a single independent realization of the stirring sequence. That is, typically  $N_{\text{B}} = 1$  for this term.

It is typically necessary to average each measurement sample over many transmitted symbols (or bursts, blocks or frames, depending on the type of communication signal) to obtain a valid estimate of the power corresponding to that sample. The duration required for each measurement sample will depend on the modulation and transmission format of the radio-access technology for the particular measurement. These measurement parameters are described in OTA test plans such as [15, 54].

As mentioned, loading is not critical for TRP measurements, but if the chamber is loaded, then averaging over position is critical. We have seen the importance of position stirring in Section 5.1.2.

In [40], the TRP of a wireless router transmitting with wideband code-division multiple access (W-CDMA) was measured in the Cellular (800 – 900 MHz and Personal Communication Service (PCS) (1.85 – 2.0 GHz) bands at uplink frequencies of 1.85-1.854, respectively. Agreement between the reverberation chamber measurement and two different anechoic chambers was within 2 dB, which is the CTIA limit for TRP.

### 5.2.2 Total Isotropic Sensitivity

TIS is a measure of receiver sensitivity of a wireless device derived from OTA measurements. This metric quantifies the amount of spatially averaged RF power that must be incident on a device's receive antenna to achieve a defined minimum standard of data fidelity in an isotropic environment. As with TRP, this measurement may be made in both anechoic or reverberation chamber set-ups. The BSE first establishes a communication link with a wireless device and sends a known sequence of bits as a preamble. The device then sends back the bits it reads from the preamble (typically at full DUT power) and the error rate is computed at each mode-stirring step. This “error rate” may be the bit error rate, block error rate, frame error rate, or

other, depending on the transmission protocol. The BER tends to increase gradually as the power level of the BSE is lowered.

To find the device's receiver sensitivity for each spatial sample, the RF power emitted by the BSE is reduced in successive measurement steps and the error rate is again computed. This procedure continues until the minimum power required at the device is reached that is necessary to maintain a specified error rate below a given threshold. For example, in [54], this threshold is 1.2% BER for the W-CDMA transmission protocol.

A schematic representation of the TIS measurement concept is shown in Figure 5.13. Since the estimated value of TIS is based on the power incident on the DUT's receive antenna, the measurement requires a determination of the power emitted by a base-station emulator,  $P_{\text{BSE}}$ , and corrections for the power lost between the BSE and the DUT. As depicted in Figure 5.13, these losses could be due to cable loss,  $G_{\text{CableLoss}}$ , power that is not transmitted by the antenna due to impedance mismatch at the antenna port, and reference power transfer function,  $G_{\text{Ref}}$  (5.1) from Section 5.1.1. Procedures for performing TIS tests have been developed for anechoic and reverberation chambers [54, 59], but we will present the reverberation chamber method [15, 60] here.

The procedure for estimating the TIS of a wireless device from a reverberation chamber measurement is similar to that for an anechoic chamber measurement, except that instead of averaging over angular orientations of the DUT as in the anechoic chamber case, the measurements are averaged over the changing boundary conditions provided by the mode-stirring sequence.

For a given stepped mode-stirring sample,  $n$ , the power emitted from the BSE that yields the threshold error rate,  $P_{\text{BSE}}(n)$ , is recorded. Normally, the measurements for  $G_{\text{Ref}}$  are averaged over the stirring sequence in advance. If, instead, the reference and  $P_{\text{BSE}}$  samples were taken in precisely the same configuration (for example by use of a switch between the reference and DUT antennas as was done in [17]), then the TIS power,  $P_{\text{TIS}}$ , may given by

$$P_{\text{TIS}} = \frac{\eta_{\text{M}}(1-|\Gamma_{\text{M}}|^2)}{N_{\text{W}}|1-\Gamma_{\text{M}}\Gamma_{\text{RX}}|^2} \sum_{n=1}^{N_{\text{W}}} G_{\text{Ref}}(n) P_{\text{BSE}}(n), \quad (5.26)$$

where  $G_{\text{Ref}}$  defined in (5.1) has not yet been averaged,  $N_{\text{W}}$  is the number of samples in the mode-stirring sequence, and corrections have been made for the efficiency and free-space reflection coefficient of the measurement antenna and the impedance mismatch between the measurement antenna and receiver. As for TRP, we assume that the measurement antenna is identical for the measurement of  $P_{\text{BSE}}$  and  $G_{\text{Ref}}$  and that  $G_{\text{Ref}}$  provides a reasonable estimate of  $G_{\text{DUT}}$ . Even though the reference and DUT measurements are made with different antennas, when the radiation patterns are similar, the measured results will be similar [4, 33].

The TIS measurement is intended to estimate the true, intrinsic receiver sensitivity of a wireless device. Since the sensitivity is intrinsic to the DUT, the value of  $P_{\text{BSE}}$  is dependent on the value of the chamber's reference power transfer function [here termed  $G_{\text{Ref}}(n)$ ] for each mode-stirring sample. That is, at step  $n$  in the stirring sequence, if the sample of  $G_{\text{Ref}}$  goes up,  $P_{\text{BSE}}$  should ideally compensate by going down. This dependence is illustrated in Figure 5.14, which shows a plot of  $P_{\text{BSE}}(n)$  overlaid with a plot of  $G_{\text{Ref}}(n)$  averaged over a 4 MHz bandwidth, centered at 1932.4 MHz. The  $G_{\text{Ref}}$  values have been offset and inverted, allowing the two

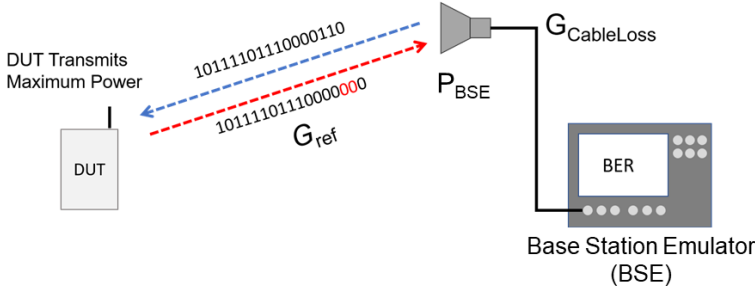


Figure 5.13: Schematic representation of a basic over-the-air measurement of TIS. The base station emulator transmits a known code sequence that is received by the DUT and transmitted back to the BSE at full power. The BSE transmit power ( $P_{BSE}$ ) is reduced until incorrect bits are sent back at a specified rate (shown in red with the red arrow). The TIS is estimated from the power incident on the DUT, so  $P_{BSE}$  is combined with any losses between the BSE and the DUT, which are shown as cable loss ( $G_{CableLoss}$ ) and any path loss ( $G_{Ref}$ ) (from [17]).

quantities to be compared. Qualitatively, the two parameters track each other very well. The uncertainty on the plotted quantities is approximately 0.5 dB [17]. Note that if the chamber loading was not sufficient, the two curves would not overlay as well.

Given the inverse dependence of  $P_{BSE}$  on  $G_{Ref}$ , as evidenced by the data in Figure 5.14, the separate averaging of the two parameters must be complimentary. To illustrate this, we recast (5.26) as

$$\frac{P_{TIS}(n)}{P_{BSE}(n)} = \frac{(1-|\Gamma_M|^2)\eta_M}{|1-\Gamma_M\Gamma_{RX}|^2} G_{Ref}(n). \quad (5.27)$$

Often, the chamber response and base station power are measured at different times and with different realizations of the mode-stirring sequence. Representing these by  $N_{W1}$  and  $N_{W2}$ , we can calculate  $P_{TIS}$  from (5.26) as

$$P_{TIS} = \frac{(1-|\Gamma_M|^2)\eta_M}{|1-\Gamma_M\Gamma_{RX}|^2} \frac{1}{N_{W1}} \left( \sum_{n_1=1}^{N_{W1}} \frac{1}{P_{BSE}(n_1)} \right)^{-1} \frac{1}{N_{W2}} \sum_{n_2=1}^{N_{W2}} G_{Ref}(n_2). \quad (5.28)$$

Eqn. (5.28) utilizes the arithmetic mean of the chamber's reference power transfer function, as was done in (5.1) in Section 5.1.2, and the harmonic mean (with inverse averaging) for the receiver sensitivity power. This is not a unique choice of averaging. That is, theoretically, the assignment of arithmetic and harmonic mean could be swapped, or the median of each quantity used. The measurement and uncertainty dependence on these choices was discussed in [60], where it was shown that the combination in (5.28) yields the most stable results.

As was mentioned, in practice [15], the measurement of  $G_{Ref}$  is carried out in a pre-characterization step of the reverberation-chamber configuration to determine proper loading and to calculate the uncertainty due to lack of spatial uniformity. This step is seldom performed again. The  $P_{BSE}$  measurement is then performed quickly

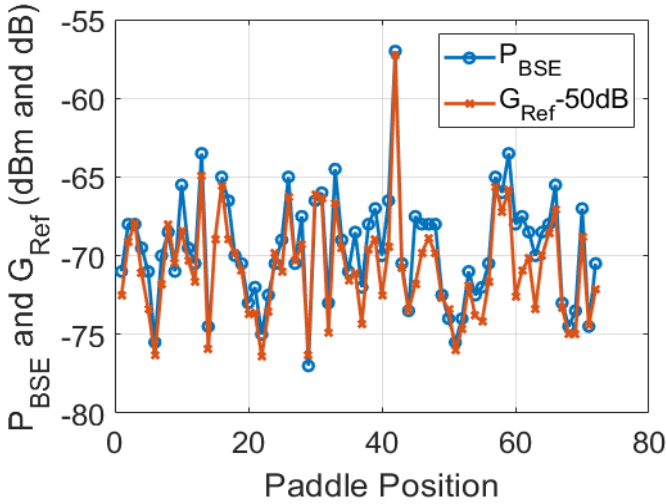


Figure 5.14: Plot of individual samples of  $P_{BSE}$  (blue) and of  $G_{ref}$  (red) vs paddle angle for a single mode-stirring sequence. The chamber was sufficiently loaded with RF absorber to produce the ideal inverted behaviour between the two parameters. For comparison, the  $G_{ref}$  has had 50 dB subtracted and has been inverted (from [17]).

on customer-provided DUTs and combined with the pre-characterization parameters to yield the TIS of each device.

As stated in the introduction, the measurement of metrics such as TIS in which the communication signal must be demodulated motivates the heavy loading of the reverberation chamber for testing of wireless devices, because the coherence bandwidth must be sufficiently wide to provide a frequency flat channel. Figure 5.15 shows measured examples of TIS as a function of chamber loading for two different reverberation chambers. The chamber with the larger error bars utilized a single mode-stirring paddle and no position stirring. The other chamber utilized two rotating paddles, and a turntable for position stirring, resulting in smaller error bars. Both chambers demonstrate a “plateau” in TIS for CBW values greater than the 3.84 MHz bandwidth of the W-CDMA communications signal. This again illustrates the need for heavy loading of the chamber for OTA measurements of wireless devices.

One key advantage of the reverberation chamber over the anechoic chamber method is that a significant fraction of the volume of the chamber is the working volume. Thus, the same chamber setup can be used to measure devices as small as printed circuit boards, to DUTs as large as trash compactors [2, 40]. The key limitation is that this setup is only useful for spatially averaged metrics of interest since angle-of-arrival information is lost. Obtaining a sufficiently wide coherence bandwidth may be another limitation, depending on the characteristics of the

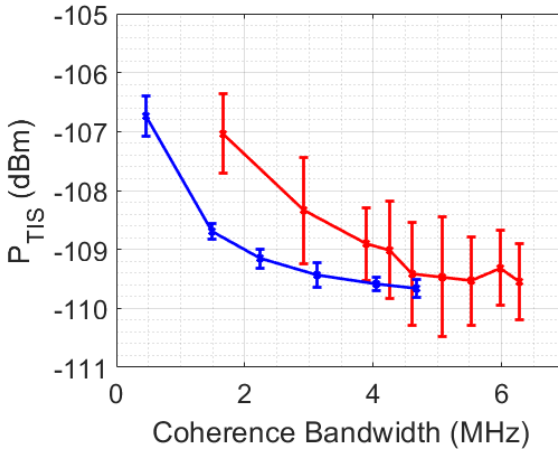


Figure 5.15: TIS power of a cellular-enabled wireless router operating in the 1.85 GHz to 2.0 GHz U.S. PCS Band measured in two different reverberation chambers. The error bars represent nine independent realizations of each stirring sequence. Position stirring was not used in the chamber with the larger error bars.

chamber set-up and the bandwidth of the communications signal to be measured [61].

### 5.3 Replicating Specific Multipath Channels for OTA Test

Many OTA tests for wireless devices require the creation of specific multipath conditions, in terms of the timing between multipath components incident upon the DUT [given by the delay spread, which was defined in (5.5)], the angles from which multipath components arrive, or both. The high number of reflections in the reverberation chamber can simulate a dense multipath environment and loading can tune the decay time, for example. For channels with longer delay spreads and/or discrete multipath components, a channel emulator may be coupled to the reverberation chamber. Experimental work on using heavily loaded reverberation chambers to simulate spatial channels is ongoing. Each of these applications is briefly described in this section.

#### 5.3.1 Highly Reflective Power Delay Profiles

Some channels present a short decay time to the device. Examples include an outdoor-to-indoor building penetration scenarios, within a building, or some urban environments in which the decay time may be on the order of a few microseconds or tens to hundreds of nanoseconds. In these cases, the chamber itself can sometimes be tuned to provide a controlled OTA test environment having this same decay time. This configuration is especially appropriate when testing in a highly reflective, dense multipath conditions. An example involving tests of an LTE cellular base station in



which an urban environment is replicated by a loaded reverberation chamber is presented in [31].

Another example is presented in Figure 5.16 [10], which compares measurements of the power delay profile in an oil refinery to those in a loaded reverberation chamber. In all of these examples, the number of reflections is sufficiently high that the densely reflective power delay profile of the reverberation chamber captures the characteristics of the environment.

A third example of the use of a reverberation chamber to directly simulate a specific multipath environment is the outdoor-to-indoor channel model investigated by the CTIA and 3GPP. The model is based on measurements made in several representative urban environments. RMS delay spread values of less than 90 ns in the 700 MHz band were extracted from measured power-delay profiles [62]. An interlaboratory comparison of reverberation chambers configured to emulate this channel model was presented in [27] with 0.7 dB standard deviation between laboratories.

### 5.3.2 Longer Power Delay Profiles

When a longer delay spread, or a PDP with discrete multipath components, is to be emulated to better match measured propagation conditions, a common technique is to connect a channel emulator to the reverberation chamber (this configuration is sometimes termed “RC+CE”). The channel emulator creates multiple reflected copies of the transmitted signal, each delayed in time, amplitude, and phase according to a specified channel model. Two examples of these channel models are the “Isotropic Urban Micro (IS UMi)” and the “Isotropic Urban Macro (IS UMa),” which consist of the same power delay profile as the Spatial Channel Model Extended (SCME) UMi and UMa, although in an isotropic environment. These RC+CE models were emulated in the interlaboratory comparison of [27], with 1.25 dB standard deviation between three laboratories for the UMi model and 1.88 dB for the UMa model.

Another example of an RC+CE measurement was provided in [63], in which the power delay profile corresponding to an urban area was replicated in a reverberation chamber. Figure 5.17 shows a comparison between measurements in a non-line-of-sight environment in downtown Denver, CO, the RC+CE, and an exponential fit to the measured data.

### 5.3.3 Emulating Spatial Channels

The above examples illustrate the use of the reverberation chamber for emulating certain isotropic-channel timing characteristics. Over the years, researchers have also investigated the use of reverberation chambers to create specific non-isotropic, directional channels [23, 28, 64, 65].

As an example, in [28], a reverberation chamber was heavily loaded to create a channel having specific spatial characteristics. RF absorber placed along one wall of the reverberation chamber damped out reflections from that surface, creating a channel measurement system with a shorter, spatially controlled power delay profile.

Figure 5.18 shows results from a synthetic aperture technique that was applied to visualize the channel. These figures show the power received at the synthetic aperture array as a function of time (on the  $x$ -axis) and azimuthal angle of arrival (on

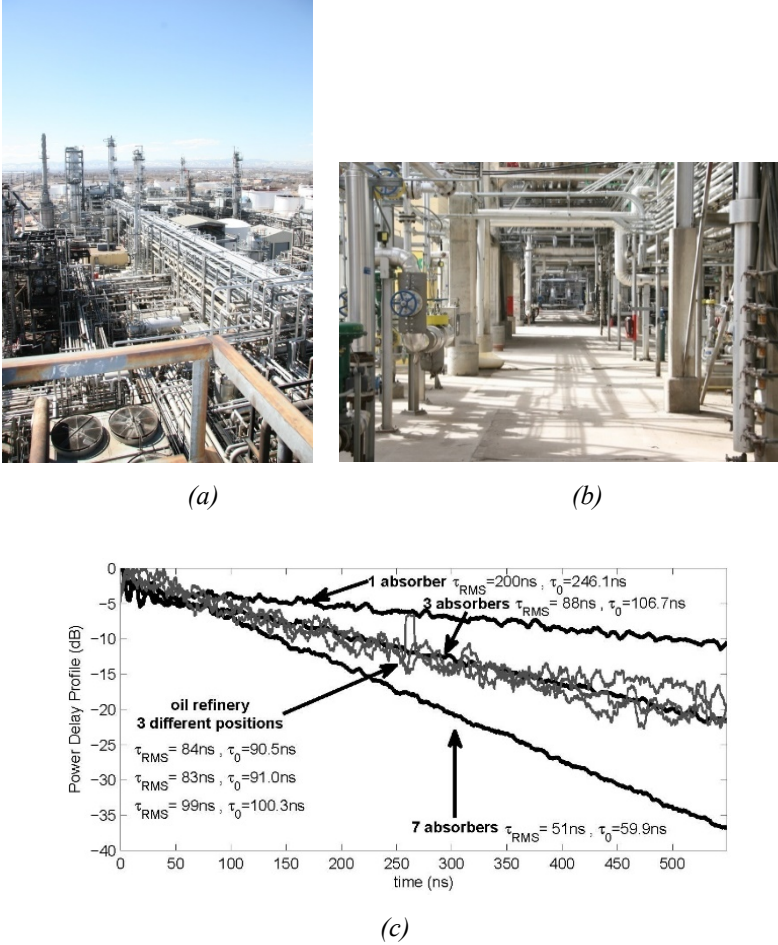


Figure 5.16: The power delay profile was measured in an oil refinery and replicated in a reverberation chamber. Photographs of the oil refinery are shown in (a) and (b), while (c) shows the chamber measurements averaged over a stirring sequence (from [10]).

the y-axis). In these figures, the received power is indicated by various colors, with red being the strongest and blue the weakest.

The unloaded chamber shown in Figure 5.18(a) shows several reflections incident on the receive antenna array from a wide range of azimuthal angles. In Figure 5.18(b), the thick red lines on the left side of the plot show the placement of the RF absorber along that wall. Reflections are damped out in that azimuthal direction and die out sooner than for the unloaded case. A controlled spatial-and-

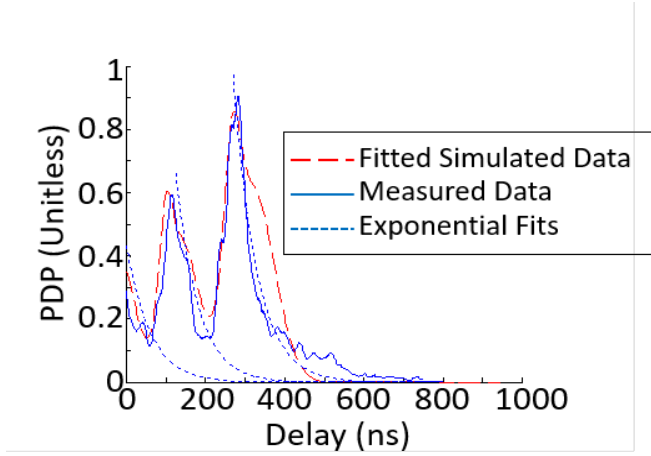


Figure 5.17: Power delay profile based on measurements from Denver, CO (blue solid line), a reverberation-chamber-plus channel emulator (red dashed line) and an exponential fit to the measured data (blue dotted line). From [63].

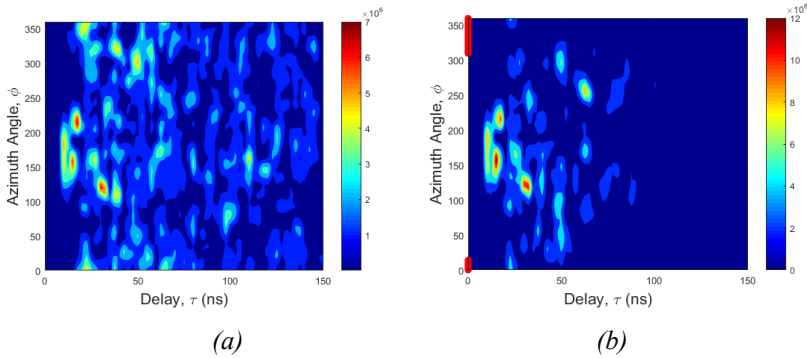


Figure 5.18: Synthetic aperture results showing reflected energy incident on a receive antenna array in (a) and unloaded reverberation chamber and (b) a reverberation chamber with RF absorber placed along the left-hand wall in the locations indicated by the thick red lines at the left of the plot (from [28]).

temporal channel test environment such as this could be useful for repeatable testing of multiple-antenna wireless devices.

## 5.4 Uncertainty in OTA Measurements with Heavily Loaded Reverberation Chambers

### 5.4.1 Number of Samples vs. Spatial Uniformity: Which Uncertainty Mechanism Dominates?

Two important sources of uncertainty in the estimate of power-based OTA metrics such as TRP and TIS derived from reverberation chambers concern the number and type of stepped mode-stirring samples used in the measurement. Understanding the origins and impact of these measurement parameters on uncertainty for OTA tests conducted in heavily loaded reverberation chambers has been a focus of this chapter. Spatial correlation due to loading reduces the effective number of mode-stirring samples. This can increase uncertainty if the mode-stirring sequence does not contain a sufficient number of uncorrelated samples. Likewise, the lack of spatial uniformity due to loading can contribute to increased uncertainty related to non-repeatable placement of the device within the working volume of the chamber. Both these effects – the limited number of mode-stirring samples and the lack of spatial uniformity – may impact the uncertainty in an estimate of OTA-derived metrics such as TRP and TIS.

For heavily loaded chambers, these two components interact, yet it is difficult to assess which dominates without further statistical analysis. For example, if a stirring sequence does not include a sufficient number of mode-stirring samples, the variance between independent realizations will be higher than if a large number of samples were used. However, it is difficult to attribute the increased variance to either the lack of mode-samples or the lack of spatial uniformity. As well, understanding which source of uncertainty dominates may lead to a simplified expression for uncertainty in reverberation-chamber measurements, which is a desirable goal for standardized test methods that strive for efficiency.

In [14], a significance test was developed that allows a user to identify which of two expressions for these components of uncertainty is most appropriate to account for these two different, yet related, sources of uncertainty.

A significance test can be used to identify the dominant source of uncertainty for a given chamber set-up, and the corresponding form that the expression for uncertainty may take [49]. The significance test in [14] may be used to identify whether statistically significant differences exist between realizations of a stirring sequence. It is based on an  $F$  distribution which is formed from the ratio of two variances [49]. To carry out this test, we first compute the variance of the samples *within* the stirring sequence

$$s_W^2 = \frac{1}{N_B(N_W - 1)} \sum_{p=1}^{N_B} \sum_{n=1}^{N_W} (G_{\text{Ref}}(n, p) - G_{\text{Ref}}(p))^2, \quad (5.29)$$

which has  $N_B(N_W - 1)$  degrees of freedom. We then compute the variance of the samples *between* multiple realizations of the stirring sequence

$$s_B^2 = \frac{N_W}{N_B - 1} \sum_{p=1}^{N_B} (G_{\text{Ref}}(p) - \hat{G}_{\text{Ref}})^2, \quad (5.30)$$

with  $N_B - 1$  degrees of freedom. (Note that the term  $N_W$  in the numerator arises from the decomposition of the sum of squares [14]). The ratio of two variances is then

formed

$$F(s_B^2, s_W^2) = \frac{s_B^2}{s_W^2}, \quad (5.31)$$

with  $N_B - 1$  and  $N_B(N_W - 1)$  degrees of freedom for the numerator and denominator, respectively.  $F_{\alpha, n_1, n_2}$  is the  $\alpha$  percentile (e.g. 95%) of the  $F$  distribution with  $n_1$  and  $n_2$  degrees of freedom.

If the test is *not significant*, that is,

$$F(s_B^2, s_W^2) < F_{0.95, N_B-1, N_B(N_W-1)}, \quad (5.32)$$

then the uncertainty due to the number of mode-stirring samples and the uncertainty due to lack of spatial uniformity both contribute to the uncertainty in the measurement of the reference. In this case, the uncertainty squared of the reference value may be given as the weighted average of  $s_B^2$  and  $s_W^2$  as

$$u_{\text{Ref}}^2 = \frac{1}{N_B N_W (N_B N_W - 1)} \sum_{n=1}^{N_W} \sum_{p=1}^{N_B} (G_{\text{Ref}}(n, p) - \hat{G}_{\text{Ref}})^2, \quad (5.33)$$

with  $N_B N_W - 1$  degrees of freedom. If the test is *significant*, then the uncertainty due to lack of spatial uniformity dominates, and the uncertainty squared in the reference value may be given as

$$\begin{aligned} u_{\text{Ref}}^2 &= \frac{1}{N_B (N_B - 1)} \sum_{j=1}^{N_B} (G_{\text{Ref}}(p) - \hat{G}_{\text{Ref}})^2 \\ &= \frac{1}{N_B} \sigma^2_{G_{\text{Ref}}} \end{aligned} \quad (5.34)$$

where the second equality is taken from (5.3) in Section 5.1.1 and with  $N_B - 1$  degrees of freedom. Note that (5.33) may considerably underestimate  $u_{\text{Ref}}^2$  when (5.34) applies. Essentially, what (5.34) states is that to correctly estimate the lack of spatial uniformity in the chamber, it is first necessary to ensure that an adequate number of mode-stirring samples are used in the stirring sequence. The reader is referred to [14] for more detail on this significance test to identify the component of uncertainty related to the reverberation chamber.

Equations (5.33) and (5.34) represent the component of uncertainty that accounts for the impact of the non-ideal reverberation chamber set-up, including number of mode-stirring samples and lack of spatial uniformity, on the estimate of  $G_{\text{Ref}}$ . The more independent realizations that are made, the lower the uncertainty in the reference measurement. For example, in [15], twelve independent realizations of  $G_{\text{Ref}}$  are measured at the edges and center of the working volume ( $N_B = 12$ ).

Both the reference measurement and the power-based measurement of the DUT ( $P_{\text{meas}}$  for TRP, Section 5.2.1, or  $P_{\text{BSE}}$  for TIS, Section 5.2.2) utilize the same OTA measurement set-up, including chamber configuration, stirring sequence and measurement antenna. Thus, this component should also be applied to the measurement of the DUT. In this case, the uncertainty squared for the DUT measurement should also account for the number of DUT measurements

$$u_{\text{DUT}}^2 \cong \frac{N_B}{N_{B, \text{DUT}}} u_{\text{Ref}}^2, \quad (5.35)$$

with the degrees of freedom corresponding to  $u_{\text{Ref}}^2$  from (5.33) or (5.34), under the assumption of independence between measurements.

While uncertainty in the reference measurement is typically estimated from multiple measurements, in practice, typically only a single measurement of the DUT is performed to save time. The smaller value of  $N_{\text{B,DUT}}$  for the DUT measurement will increase this component of uncertainty. This will be discussed further in the Section 5.4.3 on combined uncertainty.

### 5.4.2 Relative Uncertainty Due to Type of Stirring Mechanisms

As discussed in Section 5.4.1, reducing spatial correlation between samples and between mode-stirring sequences can reduce uncertainty due to the use of a non-ideal reverberation-chamber set-up. Thus, this subsection is focused on methods for reducing the reverberation-chamber-specific components of uncertainty related to spatial correlation, rather than describing a specific component of uncertainty.

As illustrated in Section 5.1.4, certain mode-stirring mechanisms more effectively stir the fields than others for a given reverberation-chamber configuration. It is possible to quantify how the selection of these mechanisms affects uncertainty using a trial-and-error, empirical approach to minimize the value of  $\sigma_{G_{\text{Ref}}}$  from (5.3). With this method, a user may design an optimal stirring sequence for a particular chamber configuration. The uncertainty due to lack of spatial uniformity will be lowest for a combination of stirring mechanisms that most efficiently stir the fields within the chamber.

More predictive approaches have been explored as well [4, 13, 38]. Using a more predictive approach, in [38], a measurement-based model of the correlation within a loaded chamber was developed and compared to the empirical approach. The correlation-based model identifies the most effective combination of mode-stirring mechanisms, providing levels of uncertainty on the order of those for an unloaded chamber with the minimal number of mode-stirring steps.

To derive the correlation-based model, the correlation coefficients between spatial mode-stirring samples are first identified. To do this, the  $S$  parameters are measured on a fine spatial grid that covers the range of stirring mechanisms to be used for a particular chamber set-up. The estimated values of the correlation terms are obtained from a single large  $M_{\text{max}} \times N_{\text{max}}$  measurement and applied to each  $M \times N$  subset stirring-sequence. Two 2D correlation matrices  $\mathbf{R}_{M_{\text{max}}}$  and  $\mathbf{R}_{N_{\text{max}}}$ , with dimensions  $M_{\text{max}} \times M_{\text{max}}$  and  $N_{\text{max}} \times N_{\text{max}}$  and elements  $r_{mm'}$  and  $r_{nn'}$ , are calculated for each stirring mechanism, respectively. The correlation coefficients  $r_M$  and  $r_N$  are then identified.

The correlation-based model takes the form [38]

$$\hat{u} = \frac{1}{\sqrt{MN}} \{[1 + (M - 1)r_M][1 + (N - 1)r_N]\}^{1/2}, \quad (5.36)$$

where a stirring sequence consists of  $M$  samples of one stirring mechanism (such as platform stirring),  $N$  samples of a second stirring mechanism (such as paddle stirring),  $r_M$  and  $r_N$  describe the correlation between samples, and  $\hat{u}$  is the relative uncertainty based on the model, defined as

$$\hat{u}^2 = \frac{\sigma^2(\langle |S_{21}|^2 \rangle_{M,N}^{(q)})}{\left(\frac{1}{Q} \sum_{q=1}^Q \langle |S_{21}|^2 \rangle_{M,N}^{(q)}\right)^2}. \quad (5.37)$$

Here,  $Q$  indicates the number of unique realizations that can be extracted from the large measurement for a given stirring sequence consisting of  $M$  antenna positions and  $N$  paddle positions. That is,  $Q = M_{\max}N_{\max}/MN$  realizations of an  $M \times N$  measurement that are collected from a large  $M_{\max} \times N_{\max}$  measurement.

The correlation coefficients are applied to yield the effective number of samples that should be used in the determination of uncertainty for a given stirring sequence. In [38], it was shown that the uncertainty could be reduced nearly to that of an unloaded chamber  $1/\sqrt{MN}$  when the optimal configuration (ratio of paddle stirring to platform stirring) was used.

To verify the model, it was compared to the empirically derived uncertainty due to lack of spatial uniformity in (5.34). For the comparison, a normalized version of the uncertainty due to lack of spatial uniformity given in (5.34) was utilized, given by

$$\sigma_{G_{\text{Ref}}, \text{norm}} = \frac{\sigma_{G_{\text{Ref}}}}{\hat{G}_{\text{Ref}}}. \quad (5.38)$$

The F test described in Section 5.4.1 was applied to ensure that the uncertainty due to lack of spatial uniformity dominated, as opposed to the number of samples within the mode-stirring sequence.

As an example from the study in [38], 60 mode-stirring samples comprised a stirring sequence. The number of paddle and platform samples were selected randomly (without replacement) from a large set of measured data that covered the range of stirring mechanisms (15 platform positions x 64 paddle positions x 4 heights). Ten ratios of platform-to-paddle samples ranging from 60:1 to 1:60 were chosen from this larger set of data. Four loading conditions were considered in three chambers, two of which are shown here.

Figures 5.19(a) and 19(b) illustrate results for the empirical uncertainty method (solid lines) and the measurement-based model (dashed lines). The data error bars correspond to the standard error over a 150 MHz frequency band and the standard

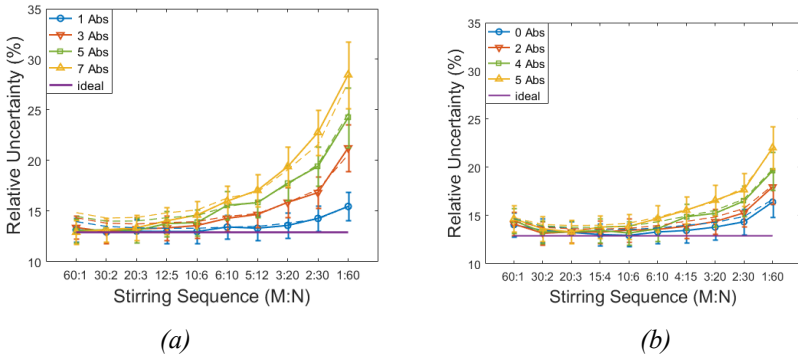


Figure 5.19: Relative mode-stirring uncertainties corresponding to selected stirring sequences with a total of  $M \times N = 60$  measurements for (a) a large dual-paddle chamber, and (b) a small dual-paddle chamber. The modeled results are shown by the dashed lines (from [38]).

deviation over 20 repeat realizations of the empirical uncertainty analysis. The “ideal” uncertainty, if no correlation existed, is shown by the horizontal line that corresponds to  $1/\sqrt{60}$  [29].

As shown in Figures 5.19(a) and 19(b), the predictive correlation-based model for uncertainty agrees well with the empirical approach. Further, the 20:3 ratio of platform-to-paddle stirring minimizes the relative uncertainty in the chamber configurations for all loading cases that were studied. The results clearly show that for both of these chambers, the use of only paddle stirring can lead to a significant increase in uncertainty. The appropriate combination of paddle and platform mode-stirring brings the uncertainty within close range of that in a chamber with no correlation between mode-stirring samples, shown by the flat line in Figures 5.19(a) and 19(b). Design rules for optimizing a stirring sequence will be different for every chamber and set of mode-stirring mechanisms. However, it is clear that position stirring must be used in loaded chambers to obtain the lowest uncertainty.

### 5.4.3 Uncertainty due to Difference in Reference and DUT Antennas

In OTA tests of wireless devices made using reverberation chambers, a reference measurement is used to estimate the reference power transfer function (chamber loss) experienced by the DUT. That is, the measurement of  $G_{\text{Ref}}$  is intended to estimate  $G_{\text{DUT}}$  because  $G_{\text{DUT}}$  cannot be directly measured on a wireless device with an integrated antenna. However, differences in the radiation pattern of the reference antenna and DUT antenna can lead to differences between  $G_{\text{Ref}}$  and  $G_{\text{DUT}}$  (if it could be measured) in a loaded reverberation chamber. This is because the reduced spatial uniformity for loaded chambers combined with the potentially limited “field of view” of directional antennas may lead to different amounts of stirred vs. unstirred energy at the antenna element. As a result, the ratio of unstirred energy to stirred energy [the K-factor, defined in (5.23)] could be different for the reference and DUT measurements. This, in turn, could result in different values of the measurement-derived reference power transfer function, as well as different correlations and uncertainties.

This effect was studied in [33], where measurements of simulated DUTs with removable antennas allowed comparison of  $G_{\text{Ref}}$  and  $G_{\text{DUT}}$  for antennas having similar and different radiation patterns. The effect was studied for a “typical” OTA test configuration for cellular device testing in a large reverberation chamber. The test configuration included the following:

- A single stepped rotating paddle (72 steps) and platform stirring (9 locations)
- Directional dual-ridge horn antenna (DRHA) measurement antenna oriented to minimize direct coupling
- Tests at PCS (1.8 – 1.95 GHz), Cell Band (800 – 900 MHz), and mmWave frequencies (43 – 47 GHz). Results are shown here for the PCS Band frequencies.
- Loading for 4 MHz coherence bandwidth for PCS. Both loaded and unloaded chambers were studied.

Several antenna types and configurations were studied, including two omnidirectional antennas (“Discone” and “Router”) and a directional antenna that was randomly oriented with respect to the measurement antenna (“DRHA RPol”). These three antenna configurations had significant direct coupling to the



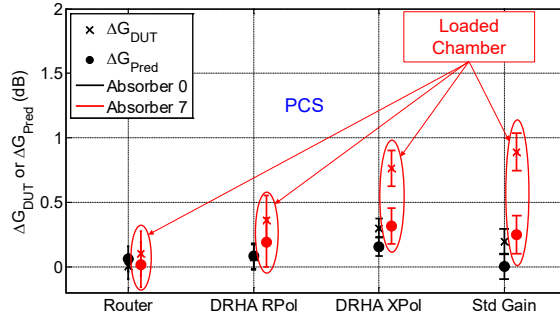


Figure 5.20: The difference between a simulated device's power transfer function  $G_{DUT}$  and either (1) the reference power transfer function  $G_{Ref}$ , given by  $(\Delta G_{DUT})$  (x's) or (2)  $G_{DUT, Pred}$  from (5.39) ( $\Delta G_{Pred}$ ) (dots). Two different loading cases are shown. 0 dB corresponds to the case where there is no error in the estimate of  $G_{DUT}$  (from [33]).

measurement antenna and, hence, significant average  $K$ -factors (averaged over the stirring sequence). Two different directional antennas were cross polarized and pointed away from the measurement antenna at each platform location to minimize unstirred, direct coupling ("DRHA XPol" and a standard gain horn "Std Gain") resulting in a lower average  $K$ -factors for these cases.

From this set of antennas, we denoted one antenna as a "DUT" antenna and measured the difference in the reference power transfer function for all other "reference" antennas. This difference was termed  $\Delta G_{DUT}$  in [33]. For the results shown in Figure 5.20, we used the discone as a DUT antenna and measured the reference power transfer function using all other antenna types. In a second case, we used the standard gain horn as the DUT and all other antennas as the reference. In this way, we could study both "similar" reference/DUT antenna pairs (e.g., omni/omni) and "different" reference/DUT antenna pairs (e.g., omni/dir).

These studies showed several effects: (1) For unloaded chambers, differences in  $G_{Ref}$  and  $G_{DUT}$  are insignificant, as shown by the small value of  $\Delta G_{DUT}$  for the "Absorber 0" cases in Figure 5.20 (the black x's). This is expected because the stirred energy dominates in unloaded chambers, which has the effect of eliminating antenna pattern [35]. (2) For loaded chambers in which the reference and DUT antennas had nominally similar radiation patterns, differences between  $G_{Ref}$  and  $G_{DUT}$  were small, as shown by the small value of  $\Delta G_{DUT}$  for the "Router" antenna (as compared to the omnidirectional discone) in the "Absorber 7" case (the red x). (3) For loaded chambers, if the antennas have different radiation patterns leading to different  $K$ -factor values, the value of  $\Delta G_{DUT}$  could be significant, ranging from 0.35 dB to 1 dB for the "Absorber 7" cases in Figure 5.20 (red x's).

To minimize this effect, current practice is to select a reference antenna that produces a  $K$ -factor that is "similar" to that of the DUT. For example, azimuthally omnidirectional reference antennas are often used to estimate  $G_{Ref}$  for testing cellular devices, which nominally radiate in all directions azimuthally.

To account for differences in the (typically unknown) DUT antenna radiation pattern and the reference antenna, certain standards groups require inclusion of a component of measurement uncertainty [15]. As an example, for current below-6 GHz wireless devices in the PCS band, an omnidirectional-DUT/directional-reference pattern mismatch could lead to up to 0.35 dB error (corresponding to an error in power of 0.084), as shown by the second-from-the-left red x's in Figure 5.20. If we assume that a less-directional reference antennas would typically be used, we may consider 0.35 dB a worst-case bound. The systematic uncertainty component  $u_K$  would then be uniformly distributed, with a standard deviation of  $u_K = \sigma_K \approx 0.084/\sqrt{12} \approx 0.1$  dB [49].

If the user has access to the DUT's antenna ports and the  $K$ -factor,  $\kappa$ , associated with a measurement of the wireless device in a specific chamber configuration can be determined, a correction factor can be calculated to minimize the differences in transfer function values [33]. In this case, the DUT transfer function can be written as

$$G_{\text{DUT, Pred}} = G_{\text{Ref}}^{\frac{1+\kappa_D}{1+\kappa_R}}, \quad (5.39)$$

where  $\kappa_D$  and  $\kappa_R$  are the  $K$ -factors for the DUT and reference measurements, respectively, averaged over a stirring sequence. One may obtain an improved estimate of the wireless metrics TRP and TIS by using  $G_{\text{DUT, Pred}}$  in place of  $G_{\text{Ref}}$  if the  $K$ -factors are known. In either case, obtaining this value of uncertainty is complicated and still a topic of research in the community. Its importance will likely become more significant as directional antennas are used in future wireless systems.

#### 5.4.4 Combined and Expanded Uncertainties

We have identified three components of uncertainty that are specifically due to the use of reverberation chambers in wireless OTA tests: The uncertainties  $u_{\text{Ref}}$  and  $u_{\text{DUT}}$  arising from the nonidealities associated with reverberation-chamber measurements, including both the limited number of samples in a stepped mode-stirring sequence and the lack of spatial uniformity in the chamber set-up (Section 5.4.1), and the uncertainty due to the difference in reference and DUT antenna type (Section 5.4.3),  $u_K$ . In the final uncertainty analysis, there will be many other components of uncertainty, such as those related to the measurement equipment and the estimated antenna efficiency. But, for an example, we illustrate combination of these three.

These components may be combined using a root-sum-of-square approach as

$$\begin{aligned} u_{\text{Combined}}^2 &= \sqrt{u_{G_{\text{Ref}}}^2 + u_{\text{DUT}}^2 + u_K^2}, \\ &= \sqrt{\frac{1}{N_B} \sigma_{G_{\text{Ref}}}^2 + \frac{1}{N_{\text{DUT}}} \sigma_{\text{DUT}}^2 + \sigma_K^2} \end{aligned} \quad (5.40)$$

with the number of degrees of freedom for the first two terms corresponding to (5.33) or (5.34) from Section 5.4.1. We assume that the degrees of freedom for the systematic error  $u_K$  is infinite [66]. Because the components have different degrees

of freedom, we use the Welch-Satterthwaite equation to find the effective degrees of freedom due to the pooled variance as [66]

$$\nu_{\text{eff}} \cong \frac{(\sum_{i=1}^n k_i u_i^2)^2}{\sum_{i=1}^n \frac{(k_i u_i^2)^2}{\nu_i}}, \quad (5.41)$$

where

$$k_i = \frac{1}{\nu_i + 1}.$$

Because the systematic uncertainty term is assumed to have infinite degrees of freedom, this term drops out from the summations in (5.41). Substituting  $\nu_1 = \nu_2 = N_B - 1$  and  $k_1 = k_2 = \frac{1}{N_B}$  into (5.41) and simplifying, we end up with an effective number of degrees of freedom of

$$\nu_{\text{eff}} \cong \frac{\left(\frac{1}{N_B} + \frac{1}{N_{\text{DUT}}}\right)^2}{\left(\frac{1}{N_B}\right)^2 + \left(\frac{1}{N_{\text{DUT}}}\right)^2} (N_B - 1). \quad (5.42)$$

To find the expanded uncertainty  $U_{95}$  corresponding to a 95 % confidence level, the coverage factor  $k_{95}$  is determined from the effective degrees of freedom from (5.42). The number of degrees of freedom is then used to calculate the coverage factor  $k_{95}$  as recommended in Appendix B3 of [49]. That is,  $k_{95} = t_{95}(\nu)$ , where  $t_{95}(\nu)$  is the two-sided 95<sup>th</sup> percentile of the Student's  $t$ -distribution having  $\nu$  degrees of freedom. Note that, depending on the number of measured samples of  $N_B$  and  $N_{\text{DUT}}$ ,  $\nu$  can be small. This would make the coverage factor larger than two. Finally,  $U_{95}$  is found as

$$U_{95, \text{Combined}} = k_{95} u_{\text{Combined}}. \quad (5.43)$$

## 5.5 Conclusion

In this chapter, we covered some of the key issues related to the use of heavily loaded reverberation chambers for OTA testing of wireless device performance. Specifically, we addressed cases where the communication signal is spread over a wide modulation bandwidth and must be demodulated and cases in which a particular power delay profile is to be replicated. Metrics used to characterize the chamber configuration, such as the reference power transfer function, spatial uniformity, isotropy and chamber decay time are not significantly different from those used in prior work of the EMC/EMI community. However, their application to the case where significant correlation exists between frequencies and spatial samples requires additional consideration. As such, we paid a great deal of attention to the assessment correlation and its impact on uncertainty in the estimate of power-based metrics such as TRP or TIS.

Throughout, we attempted to provide the theoretical basis for current standardized test approaches of cellular wireless devices, including a summary of the OTA test methods currently used for TRP and TIS from single-antenna devices. We briefly touched on the use of reverberation chambers in the emulation of specific multipath channels. This is expected to be a growth area in the future as wireless devices more commonly use multiple antenna systems designed for optimal

operation in multipath environments. Such environments are provided naturally by the reverberation chamber.

Finally, we provide a summary of components of uncertainty specifically related to the use of heavily loaded reverberation chamber for OTA test of wireless devices. While this development focused on cellular-enabled wireless devices, the techniques and uncertainty analyses can be extended to other types of wireless devices in a straightforward way. With the increased prevalence of wireless devices for internet-of-things and machine-to-machine communications, we anticipate that the use of reverberation chamber methods for efficient OTA test will continue to grow in the years ahead.

## 5.6 Acknowledgements

The authors are grateful for the contributions of current and former NIST colleagues and affiliates including Chris Holloway, John Ladbury, Ben Jamroz, Dylan Williams, Michael Frey, Maria Becker, Ryan Pirkel, Damir Senic, Robert Jones, Stephan van de Beek, Joop Ann Den Toorn, Jos Dortmans, Anouk Hubrechson, Thomas Meurs, Matt North, Vincent Neylon, Christian Lotback, Haider Shah and Arvand Homer.

## References

- [1] Andrieu G, Ticaud N, Lescoat F, et al. Fast and Accurate Assessment of the “Well Stirred Condition” of a Reverberation Chamber From  $S_{11}$  Measurements. *IEEE Trans Electromagn Compat.* 2019;61(4):974-82.
- [2] Chen X, Kildal P, Orlenius C, et al. Channel Sounding of Loaded Reverberation Chamber for Over-the-Air Testing of Wireless Devices: Coherence Bandwidth Versus Average Mode Bandwidth and Delay Spread. *IEEE Antennas Wireless Propag Lett.* 2009;8:678-81.
- [3] Remley KA, Floris SJ, Shah HA, et al. Static and Dynamic Propagation-Channel Impairments in Reverberation Chambers. *IEEE Trans Electromagn Compat.* 2011;53(3):589-99.
- [4] Kildal P, Chen X, Orlenius C, et al. Characterization of Reverberation Chambers for OTA Measurements of Wireless Devices: Physical Formulations of Channel Matrix and New Uncertainty Formula. *IEEE Trans Antennas Propag.* 2012;60(8):3875-91.
- [5] Corona P, Ferrara G, Migliaccio M. Reverberating chamber electromagnetic field in presence of an unstirred component. *IEEE Trans Electromagn Compat.* 2000;42(2):111-5.
- [6] Hill DA, Ladbury JM. Spatial-correlation functions of fields and energy density in a reverberation chamber. *IEEE Trans Electromagn Compat.* 2002;44(1):95-101.
- [7] Orlenius C, Kildal P, Poilasne G. Measurements of total isotropic sensitivity and average fading sensitivity of CDMA phones in reverberation chamber. 2005 *IEEE Antennas and Propagation Society International Symposium*; 3-8 July 2005. p. 409-12 Vol. 1A.
- [8] Holloway CL, Hill DA, Ladbury JM, et al. On the Use of Reverberation

- Chambers to Simulate a Rician Radio Environment for the Testing of Wireless Devices. *IEEE Trans Antennas Propag.* 2006;54(11):3167-77.
- [9] Delangre O, Doncker PD, Lienard M, et al. Delay spread and coherence bandwidth in reverberation chamber. *Electron Lett.* 2008;44(5):328-9.
- [10] Genender E, Holloway CL, Remley KA, et al. Simulating the Multipath Channel With a Reverberation Chamber: Application to Bit Error Rate Measurements. *IEEE Trans Electromagn Compat.* 2010;52(4):766-77.
- [11] Sanchez-Heredia JD, Gruden M, Valenzuela-Valdes JF, et al. Sample-Selection Method for Arbitrary Fading Emulation Using Mode-Stirred Chambers. *IEEE Antennas Wireless Propag Lett.* 2010;9:409-12.
- [12] Chen X. Experimental Investigation of the Number of Independent Samples and the Measurement Uncertainty in a Reverberation Chamber. *IEEE Trans Electromagn Compat.* 2013;55(5):816-24.
- [13] Remley KA, Pirkel RJ, Shah HA, et al. Uncertainty From Choice of Mode-Stirring Technique in Reverberation-Chamber Measurements. *IEEE Trans Electromagn Compat.* 2013;55(6):1022-30.
- [14] Remley KA, Wang CJ, Williams DF, et al. A Significance Test for Reverberation-Chamber Measurement Uncertainty in Total Radiated Power of Wireless Devices. *IEEE Trans Electromagn Compat.* 2016;58(1):207-19.
- [15] CTIA Certification. Test Plan for Wireless Large-Form-Factor Device Over-the-Air Performance. CTIA; 2019.
- [16] Orlenius C, Franzen M, Kildal P, et al. Investigation of Heavily Loaded Reverberation Chamber for Testing of Wideband Wireless Units. 2006 IEEE Antennas and Propagation Society International Symposium; 9-14 July. p. 3569-72.
- [17] Horansky RD, Remley KA. Flexibility in Over-the-Air Testing of Receiver Sensitivity With Reverberation Chambers. *IET Microw Antenna P.* 2019.
- [18] Wolfgang A, Orlenius C, Kildal P. Measuring output power of Bluetooth devices in a reverberation chamber. *IEEE Antennas and Propagation Society International Symposium Digest Held in conjunction with: USNC/CNC/URSI North American Radio Sci Meeting (Cat No03CH37450)*; 22-27 June 2003. p. 735-8 vol.4.
- [19] Monebhurrin V, Letertre T. Total radiated power measurements of WiFi devices using a compact reverberation chamber. 2009 20th International Zurich Symposium on Electromagnetic Compatibility; 12-16 Jan. 2009. p. 65-8.
- [20] Rudander JH, Ikram e K, Kildal P, et al. Measurements of RFID Tag Sensitivity in Reverberation Chamber. *IEEE Antennas Wireless Propag Lett.* 2011;10:1345-8.
- [21] Svedjenäs P, Dong W, Arvidsson K, et al. OTA device sensitivity in the presence of interference measured in a reverberation chamber. 2014 International Symposium on Electromagnetic Compatibility; 1-4 Sept. 2014. p. 328-31.
- [22] Delangre O, Doncker PD, Horlin F, et al. Reverberation Chamber Environment for Testing Communication Systems: Applications to OFDM and SC-FDE. 2008 IEEE 68th Vehicular Technology Conference; 21-24 Sept. 2008. p. 1-5.
- [23] Valenzuela-Valdes JF, Martinez-Gonzalez AM, Sanchez-Hernandez DA. Emulation of MIMO Nonisotropic Fading Environments With Reverberation Chambers. *IEEE Antennas Wireless Propag Lett.* 2008;7:325-8.
- [24] Kildal P, Rosengren K. Correlation and capacity of MIMO systems and mutual coupling, radiation efficiency, and diversity gain of their antennas: simulations and measurements in a reverberation chamber. *IEEE Communications Magazine.* 2004;42(12):104-12.

- [25] Valenzuela-Valdes JF, Garcia-Fernandez MA, Martinez-Gonzalez AM, et al. The Influence of Efficiency on Receive Diversity and MIMO Capacity for Rayleigh-Fading Channels. *IEEE Trans Antennas Propag.* 2008;56(5):1444-50.
- [26] Kildal P, Orlenius C, Carlsson J. OTA Testing in Multipath of Antennas and Wireless Devices With MIMO and OFDM. *Proc IEEE.* 2012;100(7):2145-57.
- [27] Mora-Andreu M, Sánchez-Hernández DA. Reverberation Chamber results on 3GPP/CTIA LTE MIMO OTA 2013 round robin tests using different channel models — A comparison of performance. *The 8th European Conference on Antennas and Propagation (EuCAP 2014)*; 6-11 April 2014. p. 3684-7.
- [28] Becker MG, Horansky RD, Senic D, et al. Spatial channels for wireless over-the-air measurements in reverberation chambers. *12th European Conference on Antennas and Propagation (EuCAP 2018)*; 9-13 April 2018. p. 1-5.
- [29] Kostas JG, Boverie B. Statistical model for a mode-stirred chamber. *IEEE Trans Electromagn Compat.* 1991;33(4):366-70.
- [30] Hussain A, Kildal P. Study of OTA throughput of LTE terminals for different system bandwidths and coherence bandwidths. *2013 7th European Conference on Antennas and Propagation (EuCAP)*; 8-12 April 2013. p. 312-4.
- [31] Micheli D, Barazzetta M, Carlini C, et al. Testing of the Carrier Aggregation Mode for a Live LTE Base Station in Reverberation Chamber. *IEEE Trans Veh Technol.* 2017;66(4):3024-33.
- [32] Holloway CL, Shah HA, Pirkil RJ, et al. Reverberation Chamber Techniques for Determining the Radiation and Total Efficiency of Antennas. *IEEE Trans Antennas Propag.* 2012;60(4):1758-70.
- [33] Remley KA, Pirkil RJ, Wang C, et al. Estimating and Correcting the Device-Under-Test Transfer Function in Loaded Reverberation Chambers for Over-the-Air Tests. *IEEE Trans Electromagn Compat.* 2017;59(6):1724-34.
- [34] Lemoine C, Besnier P, Drissi M. Investigation of Reverberation Chamber Measurements Through High-Power Goodness-of-Fit Tests. *IEEE Trans Electromagn Compat.* 2007;49(4):745-55.
- [35] Hill DA. *Electromagnetic Fields in Cavities: Deterministic and Statistical Theories.* Piscataway, NJ, USA: Wiley-IEEE Press; 2009.
- [36] Chen X, Kildal P, Lai S. Estimation of Average Rician K-Factor and Average Mode Bandwidth in Loaded Reverberation Chamber. *IEEE Antennas Wireless Propag Lett.* 2011;10:1437-40.
- [37] van de Beek S, Remley KA, Holloway CL, et al. Characterizing large-form-factor devices in a reverberation chamber. *2013 International Symposium on Electromagnetic Compatibility*; 2-6 Sept. 2013. p. 375-80.
- [38] Becker MG, Frey M, Streett S, et al. Correlation-Based Uncertainty in Loaded Reverberation Chambers. *IEEE Trans Antennas Propag.* 2018;66(10):5453-63.
- [39] Jakes WC. *Multipath Interference.* In: Jakes WC, editor. *Microwave Mobile Communications.* New York, USA: IEEE Press; 1974.
- [40] Remley KA, Dortmans J, Weldon C, et al. Configuring and Verifying Reverberation Chambers for Testing Cellular Wireless Devices. *IEEE Trans Electromagn Compat.* 2016;58(3):661-72.
- [41] Durgin GD. *Space-Time Wireless Channels.* Saddle River, NJ, USA: Prentice Hall Press; 2003.
- [42] Holloway CL, Shah HA, Pirkil RJ, et al. Early Time Behavior in Reverberation Chambers and Its Effect on the Relationships Between Coherence Bandwidth,

- Chamber Decay Time, RMS Delay Spread, and the Chamber Buildup Time. *IEEE Trans Electromagn Compat.* 2012;54(4):714-25.
- [43] Chen X. Scaling Factor for Turn-Table Platform Stirring in Reverberation Chamber. *IEEE Antennas Wireless Propag Lett.* 2017;16:2799-802.
- [44] Pirkkl RJ, Remley KA, Patane CSL. Reverberation Chamber Measurement Correlation. *IEEE Trans Electromagn Compat.* 2012;54(3):533-45.
- [45] Arnaut LR. Optimizing Low-Frequency Mode Stirring Performance Using Principal Component Analysis. *IEEE Trans Electromagn Compat.* 2014;56(1):3-14.
- [46] Burger WTC, Remley KA, Holloway CL, et al. Proximity and antenna orientation effects for large-form-factor devices in a reverberation chamber. 2013 IEEE International Symposium on Electromagnetic Compatibility; 5-9 Aug. 2013. p. 671-6.
- [47] Aan Den Toorn J, Remley KA, Holloway CL, et al. Proximity-effect test for lossy wireless-device measurements in reverberation chambers. *IET Sci Meas Technol.* 2015;9(5):540-6.
- [48] International Electrotechnical Commission. IEC 61000-4-21 Electromagnetic Compatibility (EMC) – Part 4-21: Testing and Measurement Techniques – Reverberation Chamber Test Methods. 2nd Edition ed2011.
- [49] Joint Committee for Guides in Metrology. Evaluation of Measurement Data—Guide to the Expression of Uncertainty in Measurement. Sevres, France: International Bureau of Weights and Measures (BIPM); 2008 September, 2008.
- [50] Arnaut LR. Operation of electromagnetic reverberation chambers with wave diffractors at relatively low frequencies. *IEEE Trans Electromagn Compat.* 2001;43(4):637-53.
- [51] Kildal P-S, Carlsson C. Detection of a polarization imbalance in reverberation chambers and how to remove it by polarization stirring when measuring antenna efficiencies. *Microwave and Optical Technology Letters.* 2002;34(2):145-9.
- [52] Morrison DF. *Multivariate Statistical Methods.* New York: McGraw-Hill Book Company; 1967.
- [53] NIST/SEMATECH. e-Handbook of Statistical Methods, Section 1.3.5.15 “Chi-Square Goodness-of-Fit Test.” 2012. Available from: <http://www.itl.nist.gov/div898/handbook/eda/section3/eda35f.htm>.
- [54] CTIA Certification. Test Plan for Wireless Device Over-the-Air Performance. 2018.
- [55] Chen X, Kildal P, Carlsson J, et al. Comparison of Ergodic Capacities From Wideband MIMO Antenna Measurements in Reverberation Chamber and Anechoic Chamber. *IEEE Antennas Wireless Propag Lett.* 2011;10:446-9.
- [56] Patané CL, Skårbratt A, Rehammar R, et al., editors. On the use of reverberation chambers for assessment of MIMO OTA performance of wireless devices. 2013 7th European Conference on Antennas and Propagation (EuCAP); 2013 8-12 April 2013.
- [57] Krauthausen HG. On the Measurement of Total Radiated Power in Uncalibrated Reverberation Chambers. *IEEE Trans Electromagn Compat.* 2007;49(2):270-9.
- [58] Orlenius C, Lioliou P, Franzen M, et al., Measurements of Total Radiated Power of UMTS Phones in Reverberation Chamber. The Second European Conference on Antennas and Propagation, EuCAP 2007; 2007 11-16 Nov. 2007.
- [59] Qi Y, Yang G, Liu L, et al. 5G Over-the-Air Measurement Challenges:

Overview. IEEE Trans Electromagn Compat. 2017;59(6):1661-70.

[60] Horansky RD, Meurs TB, North MV, et al., Statistical Considerations for Total Isotropic Sensitivity of Wireless Devices Measured in Reverberation Chambers. 2018 International Symposium on Electromagnetic Compatibility (EMC EUROPE); 2018 27-30 Aug. 2018.

[61] Senic D, Remley KA, Wang CJ, et al. Estimating and Reducing Uncertainty in Reverberation-Chamber Characterization at Millimeter-Wave Frequencies. IEEE Trans Antennas Propag. 2016;64(7):3130-40.

[62] Matolak DW, Remley KA, Holloway C, et al. Outdoor-to-Indoor Channel Dispersion and Power-Delay Profile Models for the 700-MHz and 4.9-GHz Bands. IEEE Antennas Wireless Propag Lett. 2016;15:441-3.

[63] Fielitz H, Remley KA, Holloway CL, et al. Reverberation-Chamber Test Environment for Outdoor Urban Wireless Propagation Studies. IEEE Antennas Wireless Propag Lett. 2010;9:52-6.

[64] Rosengren K, Kildal P. Theoretical study of angular distribution of plane waves in a small reverberation chamber for simulating multipath environment and testing mobile phones. IEEE Antennas and Propagation Society International Symposium 2001 Digest Held in conjunction with: USNC/URSI National Radio Science Meeting (Cat No01CH37229); 2001 8-13 July 2001.

[65] Pirkel RJ, Remley KA. Experimental Evaluation of the Statistical Isotropy of a Reverberation Chamber's Plane-Wave Spectrum. IEEE Trans Electromagn Compat. 2014;56(3):498-509.

[66] NIST/SEMATECH. e-Handbook of Statistical Methods 2019 [Available from: <https://www.itl.nist.gov/div898/handbook>].